SLAC-2256
UCLA-1120
February 1979
(T/E)

THE PRODUCTION OF $\bar{n}$'S AND $\bar{\Sigma}^{\pm}$'S IN e^+e^- ANNIHILATIONS**

T. Ferguson, C. Buchanan, L. Nodulman and R. Poster*
University of California at Los Angeles
Los Angeles, California 90024

and

M. Breidenbach, C. C. Morehouse† and F. Vannucci‡
Stanford Linear Accelerator Center
Stanford University, Stanford, California 94305

(To be published in Physical Review D)

**Work supported by the Department of Energy under Contract Number EY-76-C-03-0515

ABSTRACT

The production of anti-neutrons and charged anti-sigmas in e^+e^- annihilations has been measured at $\sqrt{s}$ = 4 GeV and 7 GeV and at the ψ (3.1) resonance. Two packages containing spark chambers, steel plates, and scintillation counters were added to each side of the Mark I detector at SPEAR.

Anti-neutrons were identified by annihilations which produced large angle charged prongs characteristic of a high-Q reaction. The resulting anti-neutron cross sections and momentum distributions are consistent with previous anti-proton results.

Charged anti-sigmas were detected by forming mass combinations with the $\bar{n}$'s and charged tracks in the Mark I. A clear signal is seen in the 7 GeV and ψ data, with little or no signal at $\sqrt{s}$ = 4 GeV. The increase in $\bar{\Sigma}^{\pm}$ production between 4 and 7 GeV is consistent with simple expectations for charmed baryon production.

A search for the decays $\bar{\Lambda}_c^- \to \bar{\Sigma}^{\pm} \pi^{\mp} \pi^-$ and $\bar{\Sigma}_c^* / \bar{\Sigma}_c \to \bar{\Lambda}_c^- \pi^{\pm}$ yields no significant peaks. An upper limit, at the 90% confidence level, of $\sigma_{\bar{\Lambda}_c} \times BR(\to \bar{\Sigma}^{\pm} \pi^{\mp} \pi^-) < 56$ pb is set.

I. INTRODUCTION

Many advances have occurred in particle physics during the last several years through the use of e^+e^- colliding beams. From the discovery of the ψ resonances[1,2] and charmed particles[3,4] to the existence of jets[5] and heavy leptons,[6] the e^+e^- interaction has proven to be a unique and sensitive tool for uncovering the basic properties of matter.

The general characteristics of e^+e^- physics have been fairly well measured for center of mass energies below 8 GeV.[7] Charged particle multiplicities, momentum distributions and total cross sections are all known. However, one of the areas where the data are still insufficient is the single identified particle production rates. Particle identification has either been over a limited momentum range or a small solid angle. In most cases only charged particles have been measured. The purpose of this experiment is to measure the production of anti-neutrons and charged anti-sigmas in e^+e^- collisions. Neither of these particles have been previously identified. The annihilation of the anti-neutron provides a unique signature to separate it from other neutral particles and also allows identification of anti-sigmas via their decay to $\bar{n}\,\pi^{\pm}$.

There are several features which make the measurement of anti-neutron production interesting. The ratio of nucleons to mesons in e^+e^- reactions is an important parameter that a successful theory should be able to predict. Furthermore, the ratio of the anti-neutron cross section to other baryon cross sections tests various symmetry and invariance rules.[8]

The measurement of $\bar{\Sigma}^{\pm}$ production provides an opportunity to determine the suppression of particle production due to increased mass and the addition of strangeness. The rate also provides information on one of the sources of $\bar{n}$'s and $\bar{p}$'s in e^+e^- events.

Finally, besides providing a clearer understanding of e^+e^- interactions in general, the measurement of anti-neutron and anti-sigma cross sections as a function of center of mass energy can show thresholds indicative of new particle production. Invariant mass distributions using the $\bar{n}$'s and $\bar{\Sigma}^{\pm}$'s can then reveal the masses of these particles.

II. EXPERIMENTAL APPARATUS

The experiment was performed at the Stanford Linear Accelerator Center (SLAC) using the colliding beam facility SPEAR.[9] Two identical packages were added to the sides of the Mark I magnetic detector in order to identify anti-neutrons by signatures involving one or more wide angle charged tracks indicative of high Q-value annihilations.

The magnetic detector, which has been described previously,[10,11] is shown in Fig. 1. It is an azimuthally-symmetric cylindrical solenoid, 3.6 m long and 3.2 m in diameter, with its axis along the beam direction. Starting from the center, it consists of two beam pipe counters, two layers of proportional chambers, four sets of double-plane magnetostrictive spark chambers, a ring of 48 timed scintillation trigger counters (T) with a resolution of σ = 0.4 nsec, an aluminum coil which produces a uniform 4 kG magnetic field parallel to the beam, a cylindrical array of 24 lead-scintillation shower counters, and finally iron flux return plates. The detector covers the full 2π in azimuthal angle and from 50° to 130° in the polar angle, giving a solid angle coverage of 65%. Charged particles bend in the plane perpendicular to the beams allowing a determination of their momentum with an accuracy of $\Delta p/p = .02 \times p(\text{GeV/c})$. The T counter timing along with this momentum measurement, gives a separation for $\pi/K/p$ up to 0.6 GeV/c and K/p up to 1.0 GeV/c.[12]

In the coordinate system used for the experiment, the z axis is in the direction of the positron beam, the y direction is vertical, and the x axis points horizontally towards the center of the ring.

The anti-neutron experiment[13] was installed by removing the two vertical flux return plates on each side of the Mark I. Two identical packages were placed directly behind the shower counters. Each package covers an octant of the Mark I and contains seven magnetostrictive spark chamber, 1.5 m high and 2.7 m long with both y and z readout. These are interspersed with four steel plates each 2.5 cm thick ($\sim$ 1/4 collision length), and followed by a vertical wall of five timed scintillation counters (A). The counters are 2.5 cm thick NE 110 scintillator and are viewed at each end by an RCA 8575 photomultiplier tube. This produces a timing resolution for each counter of σ = 0.5 nsec.

Figure 2 shows an enlargement of one anti-neutron package. Each package sits on a movable platform which allows it to be rolled out for easy maintenance. The first chamber is 2.0 m from the interaction region, while the counter wall is 2.5 m away, giving approximately a 5% solid angle coverage for each side.

III. DATA TAKING AND PRELIMINARY ANALYSIS

The experiment uses the normal Mark I event trigger.[14] This consists of a coincidence in the inner beam pipe counters, plus at least two trigger counter-shower counter combinations firing within 20 nsec of the passage of the beam bunches. The beams collide every 780 nsec and their passage is detected by a small electrostatic beam pick-up situated inside the beam pipe. A trigger generally requires at least two charged tracks with more than 200 MeV/c transverse momentum.

The anti-neutron spark chamber and scintillation counter information is read out in identical fashion to that of the Mark I and put on tape along with the rest of the magnetic detector data. The efficiencies of the spark chambers and counters are monitored on-line by extrapolating charged tracks identified by the Mark I through the packages.

Using the information from the Mark I chambers and counters all events are classified into several categories.[14,15] Cosmic rays are easily identified by their 8 nsec flight time across the detector. QED events are defined as having two oppositely charged tracks, collinear to within 10° and with momentum greater than one-half the beam energy. Electron and muon identification is done by the sum of the two shower counter pulse heights which cleanly separates the two processes.[10]

Events with three or more tracks which form a vertex within the interaction region of $R < 4$ cm in the x-y view, and $|z| < 40$ cm, are classified as multi-hadronic. Two prong events are also included in this category if their net charge is nonzero or if both momenta are greater than 300 MeV/c and acoplanar with the beam direction by at least 20°.

A total of 1.3 million Mark I triggers was taken during the running of the experiment from September 1976 until June 1977. The integrated luminosity is calculated from the number of large angle Bhabha events observed in the detector after correcting for solid angle coverage and detection efficiency. This is checked by counting rates in two sets of small counters 20 mrad above and below the beam pipe which record the number of small angle Bhabha scatters.

Table I gives the integrated luminosity and number of hadron events detected at the three center of mass energies where data were taken. The "4 GeV" data include energies from 3.7 to 4.4 GeV with 50% taken at the 4.4 GeV resonance and 36% at the 4.02 GeV enhancement.[16] The average energy is 4.2 GeV. The "7 GeV" running went from 5.7 to 7.5 GeV with an average energy of 6.8 GeV.

IV. DATA ANALYSIS

A. Trackfinding

For the anti-neutron analysis, all cosmic ray, e^+e^- and $\mu^+\mu^-$ events are first eliminated. To be submitted to the trackfinding program, the rest of

the events are required to have a total of five or more sparks in the planes of the annihilation chambers. Roughly 10% of the events satisfy this criterion.

The trackfinding program attempts to form two dimensional straight tracks from the sparks in each view of the anti-neutron chambers. A good track requires a probability of chi squared greater than 5%. In order to be kept for further analysis, an event needs at least one track in each view of the chambers in one package. Approximately 5% of the events satisfy this requirement.

These two dimensional tracks are next matched with charged tracks from the magnetic detector. The matching is done by projecting both the Mark I and the anti-neutron chamber tracks to the magnet coil radius. Figure 3 gives a plot of the differences between these projections for both the x-y and x-z views. A cut of 20 cm provides a clean matching of tracks.

Tracks in different views of the anti-neutron chambers are then matched together by comparing in which chambers their sparks are located. A point system is established where a certain combination of tracks receives one point for every chamber in common, no points for a chamber in neither track, and minus one for each chamber in one track but not the other. A positive point total is needed for a match and for multiple combinations the largest total is used.

B. Event Scanning Procedure

Computer drawn pictures are made of all events which have a track in our package which is not matched to an inner detector track and which points either to a stuck A counter or back to a fired T counter. This yields 1864 events at 4 GeV, 3725 at 7 GeV, and 1713 from the ψ data. These events are scanned by a physicist and fall into several categories. Cosmic rays which can be recognized by the stuck shower counter at the top of the Mark I and a straight track across the detector pointing to the track in the package are eliminated. Similarly, charged tracks missed by the Mark I trackfinding program and failures in the matching routine can be readily removed.

A difficult background to eliminate is due to electro-magnetic showers. Gamma rays from simple QED processes such as $e^+e^- \rightarrow e^+e^- \gamma$ can be recognized by the event topology. However, for hadronic events, the photon characteristics of prompt times in the counters, many sparks in the annihilation chambers and large pulse heights in the shower counters are used. All events remaining after the preliminary scan with times greater than 2 nsec past prompt are kept. This insures that late events, which are most probably not caused by photons, are not cut. For times less than 2 nsec past prompt, if the number of sparks associated with a track minus the number of unassociated sparks is less than -2, the event is rejected and, similarly, if greater than 3, it is kept. These limits were found by looking at events known to be caused by photons or charged tracks. For the events in between, a shower counter pulse height cut at three times minimum ionizing is used to eliminate electro-magnetic showers. After these requirements, 541, 927, and 851 events are kept from the $\sqrt{s}$ = 4 GeV, 7 GeV, and ψ data, respectively.

V. ANTI-NEUTRON PRODUCTION

A. Event Selection

The remaining events still contain a sizable photon background plus tracks caused by K_L°'s, neutrons, cosmic rays, and anti-neutrons. The anti-neutron sample is enhanced by using the fact that charged prongs from annihilations tend to be produced at large angles, while in other hadronic interactions, as well as showers, the tracks tend to be peaked in the forward direction. For events using an A counter, we demand one or more tracks in our package at angles greater than 30° from the anti-neutron direction. At this angle the anti-neutron detection efficiency is still high (see Sec. C), while the probability of a neutron, for example, producing a prong at greater than 30° is approximately

ten times less than for one in the forward direction.[17] Figure 4 shows a good anti-neutron candidate interacting in a shower counter and producing two wide-angle prongs, one of which strikes an A counter.

Since the T counters are much closer to the beams and are not shielded from photons, their background is worse. In order to keep events using their timing, we require the presence of a visible track going back into the Mark I from the region of the latched T counter, as well as a forward track at any angle into the anti-nucleon package.

To calculate the anti-neutron momentum by using the A or T counter timing, the $\bar{n}$ annihilation position must be known, as well as the time for the charged particle to travel to the counter. Since neither of these is directly measured, Monte Carlo predicted average values must be used. Tracks that have a spark in either of the first two chambers are assumed to come from annihilations in the magnetic detector. Using annihilation cross sections[18,19] and the Monte Carlo technique discussed in Sec. C, an average radius is found for anti-neutrons interacting in the Mark I. The tracks are then pointed back to this radius giving the estimate of the annihilation position. Events that do not have a spark in either the first two chambers are presumably caused by interactions in the package and the center of the steel plate in front of the first spark is used as the annihilation point.

The average β of the charged prongs which hit the counters is found by a similar method. Using the known momentum distribution for pions from anti-proton annihilations,[20-23] and the energy loss in the material of the detector, the Monte Carlo finds an average β of 0.9. The procedure is then to calculate the distance from the determined annihilation point to the counter and to subtract the time for a pion of $\beta = 0.9$ to travel this distance from the

counter timing. This gives the anti-neutron's time of flight and since it originated from the e^+e^- interaction point, its momentum vector can be found. Using this technique and the Monte Carlo program discussed in Sec. C, the anti-neutron momentum resolution is found to be

$$\Delta p/p \approx 0.15xp \text{ (GeV/c)}.$$

The resulting $\bar{n}$ momentum spectra for the three sets of data, uncorrected for background or efficiency, are shown in Fig. 5. There is a sizable number of events that give $P_{\bar{n}} > 2.0$ GeV/c or that have times faster than prompt and therefore have no $\bar{n}$ momentum. From the measured $\bar{p}$ momentum distribution,[24,26] though, we expect few anti-neutrons with momentum greater than 2.0 GeV/c. Furthermore, as will be discussed in the next sections, a large percentage of the $\bar{n}$ background should be in this range. Therefore, a cut of $P_{\bar{n}} < 2.0$ GeV/c is placed on the anti-neutron sample. This corresponds to a timing cut of approximately 1.0 nsec (2σ) past prompt.

B. Anti-Neutron Background

1. Cosmic Rays

To estimate the background from cosmic rays, computer drawn pictures were made of all events containing a track in our package that was not matched to a Mark I track and that pointed to a struck A or T counter with a time earlier than 2 nsec before prompt. These events cannot be caused by anti-neutrons and in fact are dominated by cosmic rays.

The pictures are then scanned, applying the same criteria used for the later $\bar{n}$ events, except for the time of flight cuts. Out of 228 events with an A counter timing less than 6 nsec, 12 passed the scan and had scattering angles greater than 30°. Similarly, there were 155 events with a T counter timing less than 4 nsec of which 4 faked an $\bar{n}$ event. This gives a cosmic ray background of 5.3 ± 1.5% for events using A counters and 2.6 ± 1.3% for ones

with T counters. Using these percentages and the number of identified cosmics in the correct $\bar{n}$ time of flight region, the number of expected cosmic ray background events can be obtained. Table II supplies these numbers for each of the three center of mass energies.

2. K_L^o's

The largest background and the most difficult to estimate is from K_L^o's. The inclusive cross section data[25,27] shows that the ratio of K_s^o's to $\bar{p}$'s is 3-4 at $\sqrt{s}$ = 7 GeV and as much as 6-8 at the 4 GeV enhancements where the K_s^o's are the decay products of the charmed mesons. Since the $K_L^o/\bar{n}$ ratios should be similar, there will be a large flux of K_L^o's which strike the packages. There is no efficient way of tagging these events, so the kaon background must be determined by Monte Carlo technique. The available K_L^oN cross sections and angular distributions[28] are used along with similar $K^{\pm}N$ results.[29] Produced particles such as K_s^o's and Λ^o's are allowed to decay and all final state charged prongs are tracked through the apparatus as described in Sec. C for the $\bar{n}$ Monte Carlo. The absorption of prongs in the nucleus is done following the procedure of Ref. 30.

Using the measured K_s^o momentum spectrum for each center of mass energy,[31] the Monte Carlo finds the percentage of K_L^o's which fake an $\bar{n}$ event to be 2.5% ± 1.0%. The error includes systematics caused by uncertainties in the cross sections, the angular distributions, and the absorption coefficients.

The flux of K_L^o's at each center of mass energy is calculated by assuming the inclusive K_s^o and K_L^o cross sections are equal. Combining this flux with the Monte Carlo efficiency gives the number of kaon background events, as shown in Table III. Both the number subtracted and the error are substantial

and this constitutes the largest uncertainty in determining the anti-neutron cross sections.

The Monte Carlo results are checked by looking in the $\bar{n}$ candidate events for the decay $K_S^\circ \to \pi^+\pi^-$ in the Mark I. The inclusive K_S° cross section has been measured[27] and the detection efficiency for identifying the K_S° decay in the Mark I is known.[31] If the fraction of K_S° events which also contain a K_L° is assumed to be 1/4--i.e., ignore strange baryon production and assume equal $K_S^\circ K_S^\circ$, $K_S^\circ K_L^\circ$, $K_S^\circ K^+$, $K_S^\circ K^-$ rates, then the number of events with an identified K_S° in the Mark I and a K_L° faking an anti-neutron in the package can be estimated from the Monte Carlo results. There are 8 events satisfying these criteria compared to the Monte Carlo estimate of 7.6 ± 1.7 events. Though the number of events is small, there is good agreement with the Monte Carlo predictions.

3. Photons

The gamma ray background is found by using identified photons and electrons from QED reactions--$e^+e^- \to e^+e^-$, $e^+e^-e^+e^-$, $e^+e^-\gamma$. These events are easily recognized in the Mark I and the momentum and direction of the particles are well measured. The events are submitted to the trackfinding routine and pictures are made if a track is found which points to a latched counter. These are scanned applying the same criteria as with the real $\bar{n}$ sample. Events passing the scan are analyzed with the normal $\bar{n}$ program and the number passing the scattering angle and timing cuts is found.

To convert this into a photon background, the gamma ray flux must be known. We assume that all γ's come from π°'s. Then $\langle n_\gamma \rangle = 2 \cdot \langle n_{\pi^\circ} \rangle = \langle n_{\pi^\pm} \rangle \approx \langle n_{\text{charged}} \rangle$. The photon flux can then be estimated from the published data on charged multiplicities.[7] Using these rates, the number of fake $\bar{n}$ events caused by photons is found, as shown in Table IV.

4. Neutrons

The number of background events caused by neutrons should be small since they do not have the annihilation channels of the anti-neutrons available to them. Furthermore, the charged prongs produced should be low energy since there is no longer the 1.9 GeV of energy from the annihilation of the nucleon masses. Finally, as noted in Sec. A, the neutrons tend to produce particles in the forward direction, which will not pass the 30° angular cut.

The neutron background is estimated by two independent procedures. In one, a check is made in possible anti-neutron events for protons and anti-protons which are identified in the Mark I by their time of flight. Since baryon number must be conserved in e^+e^- annihilations, if an anti-proton is found, the track in the package was probably caused by a neutron. There are 54 events with an identified proton and only 8 with an anti-proton, yielding a neutron background of 13 ± 5%.

An independent method is to compare the actual number of protons and anti-protons (again identified by their time of flight) which produce prongs greater than 30° in our package, since neutrons and anti-neutrons should behave similarly. There are 95 anti-protons satisfying this requirement and only 14 protons, again predicting a neutron background of 13 ± 4%.

Thus, after subtracting all other backgrounds, the percentage of remaining events caused by neutrons is taken to be 13 ± 3%. The final number of anti-neutrons and all background subtraction are shown in Table V.

C. Anti-Neutron Detection Efficiency

The anti-neutron detection efficiency is found by Monte Carlo technique using published data on anti-proton and anti-neutron annihilations.[18-23] The $\bar{n}$ is assumed to annihilate into an all pion final state with the pions produced isotropically in the center of mass. The pion charged multiplicity and momentum

are taken from the published data. Absorption of prongs in the nucleus is done following the procedures of Ref. 22. Pions emerging form the nucleus are tracked through the apparatus, ranging out as they go. The number of events satisfying the $\bar{n}$ criteria is then recorded. Figure 6 shows the Monte Carlo predicted efficiencies as a function of the anti-neutron momentum.

The Monte Carlo is checked by looking at the annihilation properties of anti-protons identified in the Mark I by their time of flight to the trigger counters (<1.0 GeV/c). Using the same Monte Carlo, except for the small changes due to the anti-proton's curvature in the magnetic field and energy loss in the material of the detector, the anti-proton's detection efficiency as a function of momentum is found. Using this, along with the known momentum spectrum for $\bar{p}$'s,[24] the expected number of anti-protons producing prongs in the packages is obtained. However, besides annihilating, $\bar{p}$'s may elastically or inelastically scatter, though this will usually produce prongs in the forward direction. Figure 7 shows the actual number of detected anti-protons as a function of the prongs scattering angle along with the number predicted by the Monte Carlo. At large scattering angles, where the annihilation process is dominant, there is good agreement between the experimental numbers and the Monte Carlo predictions. Furthermore, the difference between the two at small angles is well described by the angular distribution of prongs produced by protons, also shown in Fig. 7.

Since the number of observed anti-protons is rather small and the initial $\bar{p}$ flux is not exactly known, this check can not substantiate the Monte Carlo results to better than 20%. Varying the input parameters to the Monte Carlo, consistent with the available data, confirms this level of possible error.

D. Hadronic Triggering Efficiency

The efficiency for detecting hadronic events in the Mark I as a function of center of mass energy is also found by a Monte Carlo program as described in

Ref. 32. However, this is the efficiency for all hadronic events, while what is required is the efficiency for hadronic events which contain anti-neutrons. To incorporate this in the Monte Carlo is difficult since the source of $\bar{n}$'s in e^+e^- events is unclear.

The procedure used is to compare the properties of general hadronic events with those from events with an anti-neutron candidate. Charge multiplicities, single particle momentum distributions, and total momentum and energy distributions are measured at each center of mass energy. The results are given in Table VI. There is a clear decrease in all parameters for events with $\bar{n}$ candidates. This is to be expected since a larger fraction of the total energy is being taken by neutral particles. However, except for this decrease, all distributions are similar in shape to the corresponding general hadronic spectra. There is no indication of any pathological events. We thus assume that events with anti-neutrons are equivalent to general hadronic events except for this decrease in charged particle energy. The detection efficiency is then found by using the Monte Carlo generated efficiency for that center of mass energy which has the same distributions as the $\bar{n}$ events. These are given in Table VI. However, since the background is large and this method is approximate, a 20% error has been assigned to each efficiency.

E. Results and Discussion

Using the number of background subtracted anti-neutron events, along with the detection and trigger efficiencies, the fraction ($f_{\bar{n}}$) of hadronic events which contain an $\bar{n}$ is determined and thus the inclusive anti-neutron cross section ($\sigma_{\bar{n}}$). We also define

$$R_{\bar{n}} \equiv \sigma_{\bar{n}}/\sigma_{\mu\mu} = f_{\bar{n}} \cdot R \text{ where } R = \sigma_h/\sigma_{\mu\mu}$$

and σ_h and $\sigma_{\mu\mu}$ are the total hadronic and muon cross sections, respectively.

Our results are given in Table VII for the three center of mass energies. The errors quoted include both statistical and systematic uncertainties.

The values of $R_{\bar{n}}$ are plotted in Fig. 8 along with published $\bar{p}$ data.[25] The large value at the ψ reflects the fact that it is a resonance with an R_{tot} greater than 100. No other inclusive particle cross sections have been published for the ψ, so few comparisons can be made with our results. The ψ branching ratio[12] to $\bar{p}p$ of $2.2 \pm 0.2 \times 10^{-3}$ and to $\bar{N}N\pi$ of $6.2 \pm 0.5 \times 10^{-3}$ indicate that these exclusive channels are a small percentage of the ψ decays to anti-nucleons.

The DASP collaboration[33] reports the percentage of all charged prongs that are anti-protons at the ψ, as $1.8 \pm 0.5\%$. Taking the average charged multiplicity to be 3.5 ± 0.2,[7] this number corresponds to a $f_{\bar{p}} = 6.3 \pm 1.8\%$, in excellent agreement with the $f_{\bar{n}}$ result.

The $R_{\bar{n}}$ points at $\sqrt{s} = 4$ and 7 GeV are consistent with the anti-proton data.[25] However, the errors are too large to confirm the step seen in the $\bar{p}$ cross section around 4.5 GeV.

The anti-neutron and anti-proton[24,26] momentum spectra are compared in Fig. 9 for the three center of mass energies. There is good agreement in both shape and magnitude between the two anti-nucleon momentum distributions.

The invariant $\bar{n}$ and $\bar{p}$ cross sections $E\, d^3\sigma/dp^3$ are plotted in Fig. 10 for $\sqrt{s} = 7$ GeV. In statistical or hydrodynamic models[34] these cross sections should fit the universal function $\exp(-E_h/kT)$, where E_h is the hadron energy and $kT \approx 160$ MeV. The curve shown is the function $\exp(-E_h/190\ \text{MeV})$ from Ref. 24 which describes the lower momentum pion data. Within the errors, the anti-baryon cross sections are consistent with this function.

VI. ANTI-SIGMA PRODUCTION

A. $\bar{\Sigma}^{\pm}$ Mass Distributions

The detection of anti-neutrons also provides the opportunity to measure $\bar{\Sigma}^{\pm}$ production by forming effective mass combinations using the $\bar{n}$ candidates and

the charged tracks identified in the Mark I. To first reduce the background, several cuts are made on the magnetic detector charged tracks. Using the ability of the Mark I to distinguish $\pi/K/p$, protons and kaons are eliminated from the sample. The beta (β_m) of a particle can be found by measuring its path length to the T counters and its time of flight. Since the momentum is also measured, one can predict what the beta ($\beta_p = p/\sqrt{p^2 + m^2}$) should be for π, K, and p. A relative weight for each particle is calculated from

$$Wt(p) = \exp[-(\beta_m - \beta_p)^2/2 \cdot \Delta\beta_m^2]$$

where $\Delta\beta_m$ is the error in beta from the momentum and timing uncertainties. If the sum of the three weights is greater than 0.01, they are renormalized so that their sum is one. A charged track is then cut if $Wt(\pi) < 0.1$ and either $Wt(K) > 0.1$ or $Wt(p) > 0.1$. Tracks, whose closest distance of approach to the e^+e^- interaction point are inconsistent with anti-sigma decay, are also cut.

Since the anti-sigma charged states are separated in mass by 8 MeV, a relative mass spectrum is formed by subtracting the appropriate $\bar{\Sigma}^{\pm}$ mass (either 1.189 or 1.197 GeV) from each combination, depending on the charge of the pion used. To minimize multiple counting, no event is allowed to put more than one mass combination in any one bin. Figure 11 shows the spectra for the three center of mass energies. There is a clear signal centered at zero in both the 7 GeV and ψ data, with little or no signal in the 4 GeV spectrum.

To obtain the actual number of anti-sigmas from these plots, a least squares fit is performed using a polynomial for the background and a Gaussian with variable amplitude, offset, and width for the signal. Because we wish to compare production at 4 and 7 GeV, and since there is little signal in the 4 GeV data, to avoid biases the two spectra are combined for the purpose of obtaining the offset and width. Once these are found, the plots are re-fit separately to give the total number of anti-sigmas at each energy. The ψ data

is fit by itself and Table VIII gives the relevant numbers for all three center of mass energies. The widths found are consistent with the Monte Carlo predicted resolution as discussed in Sec. B.

A good check on the data is to see if there are twice as many $\bar{\Sigma}^+$'s as $\bar{\Sigma}^-$'s. This should be the case, assuming equal production of both, since $\bar{\Sigma}^+$ decays to $\bar{n}\,\pi^+$ 100% of the time while $\bar{\Sigma}^-$ decays to $\bar{n}\,\pi^-$ with only a 50% branching ratio. Figure 12 shows the two charge states separately for the 7 GeV data and the ratio of the number of $\bar{\Sigma}^+$'s (20 ± 7) to $\bar{\Sigma}^-$'s (7 ± 5) is consistent with 2.

B. Mass Resolution

The experimental anti-sigma mass resolution is found by a Monte Carlo procedure. Since the mass resolution is a strong function of the $\bar{\Sigma}^\pm$ momentum, four momentum bins of 0.0-0.5, 0.5-1.0, 1.0-1.5, and 1.5-2.0 GeV/c are picked, in which to study the resolution. Anti-sigma momenta are choosen randomly from each bin and the $\bar{n}$ and pion are produced isotropically in the $\bar{\Sigma}^\pm$ center of mass. They are transformed into the lab frame where the anti-neutron annihilates and creates prongs as discussed in Sec. V C. The pion momentum and counter timing are smeared by an amount consistent with their resolution. The $\bar{n}$ momentum is calculated the same as for real events and Fig. 13 shows the resulting $\bar{\Sigma}^\pm$ mass distributions for the four momentum bins. The rms values are σ = 3.3, 7.6, 16.8, and 20.5 MeV, respectively. Since the actual $\bar{\Sigma}^\pm$ signal is mainly in the 0.7-1.3 GeV/c range, the experimental width of $\sim$ 10 MeV is consistent with these Monte Carlo calculations.

C. Sigma Background

Neutrons from sigma decays, which interact in the packages, are the only anti-neutron background which would preferentially put events near the $\bar{\Sigma}^\pm$ mass. The percentage of neutron background has already been estimated in Sec. V B. Assuming equal sigma and anti-sigma production, this should also be the percentage of $\Sigma^\pm$ background. Therefore, the number of fitted anti-sigma events

is reduced by 13 ± 3% to account for the sigma background.

D. Results and Discussion

In analogy with the anti-neutrons, we define $f_{\bar{\Sigma}}$ as the fraction of hadronic events which contain an $\bar{\Sigma}^{\pm}$ and

$$R_{\bar{\Sigma}} = \sigma_{\bar{\Sigma}}/\sigma_{\mu\mu} = f_{\bar{\Sigma}} \cdot R,$$

where $\sigma_{\bar{\Sigma}}$ is the inclusive charged anti-sigma cross section. Table IX lists these parameters with their errors for the three center of mass energies.

The experimental values of $R_{\bar{\Sigma}}$ are shown in Fig. 14 along with the published $\bar{\Lambda}^{\circ}$ data.[25] Again, the large value at the ψ denotes its resonance character. There are no other measurements of inclusive strange baryon production at the ψ with which to compare our result. The SLAC-LBL group[12] find a $\Lambda^{\circ}\bar{\Lambda}^{\circ}$ branching ratio of $1.1 \pm 0.2 \times 10^{-3}$ and a $\Sigma^{\circ}\bar{\Sigma}^{\circ}$ fraction of $1.3 \pm 0.4 \times 10^{-3}$, showing that these exclusive channels are less than 10% of the inclusive production.

By comparing the $\bar{n}$ and $\bar{\Sigma}^{\pm}$ results, we see that anti-sigmas account for approximately 15% of the $\bar{n}$'s at the ψ and that this rises to around 30% at $\sqrt{s} = 7$ GeV. The $\bar{\Sigma}^{\pm}$ momentum spectrum for $\sqrt{s} = 7$ GeV, shown in Fig. 15, is very similar to the anti-proton[24,26] and anti-neutron distributions at this center of mass energy, which rise fairly quickly to a peak near 1.0 GeV/c and then fall slowly, with little signal beyond 2.0 GeV/c.

Within our limited statistics, we find a notable increase in $\bar{\Sigma}^{\pm}$ production between $\sqrt{s} = 4$ and 7 GeV, possibly indicative of the opening of a new channel for anti-sigma production. It is difficult to estimate the expected change due simply to the increase in center of mass energies. The anti-proton cross section,[25] for example, is remarkably flat above and below the step at 4.5 GeV. Even a factor of two increase due to this effect still leaves some remaining $\bar{\Sigma}^{\pm}$ production at the 1σ level.

This anomalous increase in $\bar{\Sigma}^{\pm}$ production between $\sqrt{s}$ = 4 and 7 GeV, coupled with the similar step in $\bar{p}$ production, is exactly what would be expected from the decays of charmed anti-baryons.

To see if these changes in $R_{\bar{\Sigma}, \bar{\Lambda}^{\circ}}$ are in agreement with simple expectations for charmed baryon production and decay, we first assume that 1/3 of the hadronic events at $\sqrt{s}$ = 7 GeV contain charmed particles. The simple ratio of the squares of the quark charges puts this fraction at 0.4. However, the presence of the heavy lepton,[6] drops the estimate slightly. The fraction of events which contain an anti-nucleon below charm threshold is $\sim$ 0.1.[24] As discussed by De Rújula, et al.,[35] though, since m_{Λ_c}/m_D = 1.2, compared to m_p/m_π = 7, and there are no form factor suppressions, this fraction should be larger for charmed events. Putting it at 0.15 and using the experimental value of R = 5.2 at $\sqrt{s}$ = 7 GeV,[7] we expect a charmed baryon production rate of

$$R_{\text{charmed baryon}} \simeq 5.2 \times 1/3 \times 0.15 = 0.26.$$

The Cabibbo favored charmed baryon decay is essentially the quark transition c $\rightarrow$ s. The strange quark must eventually appear in either a strange baryon (Σ, Λ) or a strange meson (K). There are no theoretical predictions for the relative importance of these two schemes. Assuming that they are equal, then the change in strange baryon production between 4 and 7 GeV should be

$$\Delta R_{\bar{\Sigma}, \bar{\Lambda}^{\circ}} \simeq 0.13 \times \cos^2 \theta_c = 0.12.$$

The experimental value found by combining the $\bar{\Sigma}^{\pm}$ results with the Mark I $\bar{\Lambda}^{\circ}$ data,[25] is $\Delta R_{\bar{\Sigma}, \bar{\Lambda}^{\circ}} = 0.15 \pm 0.06$. The data are therefore consistent with what would naively be expected from the decays of charmed baryons.

Assuming this anomalous strange baryon production does indeed come from the decays of charmed baryons, then an interesting comparison can be made be-

tween the $\bar{\Sigma}^{\pm}$ and $\bar{\Lambda}^{\circ}$, $\bar{\Sigma}^{\circ}$ results. Neglecting the change in inclusive particle fractions due simply to the increase in center of mass energy, a change in $\bar{\Sigma}^{\pm}$ production between 4 and 7 GeV of

$$\Delta R_{\bar{\Sigma}^{\pm}} = 0.12 \pm 0.05, \qquad (1)$$

is seen. The SLAC-LBL data give a change in $\bar{\Lambda}^{\circ}$, $\bar{\Sigma}^{\circ}$'s over the same energy range of:

$$\Delta R_{\bar{\Lambda}^{\circ},\ \bar{\Sigma}^{\circ}} = 0.027 \pm 0.01$$

It would seem reasonable that the four strange anti-baryon states $\bar{\Lambda}^{\circ}$, $\bar{\Sigma}^{+,\ -,\ \circ}$ would be equally populated from charmed anti-baryon decays. However, the ratio

$$\Delta R_{\bar{\Sigma}^{\pm}} / \Delta R_{\bar{\Lambda}^{\circ},\ \bar{\Sigma}^{\circ}} = 4.4 \pm 2.5$$

is 1.8σ from one.

Various schemes can be invented to suppress the decays of the $\bar{\Lambda}_c^-$ to $\bar{\Lambda}^{\circ}$'s relative to $\bar{\Sigma}$'s. One such idea is a large branching ratio for $\bar{\Lambda}_c^-$ to $\bar{\Lambda}$ (1405). This state decays only to $\bar{\Sigma}\pi$, thus lowering the percentage of $\bar{\Lambda}^{\circ}$'s in the final state $\bar{\Lambda}_c^-$ decay products. There is some indication for the production of $\bar{\Lambda}$ (1405) in the $\bar{\Sigma}^{\pm}\pi^{\mp}$ invariant mass plot shown in Fig. 16. Approximately 35% of the anti-sigma candidates have an $\bar{\Sigma}^{\pm}\pi^{\mp}$ mass combination within 1405 ± 25 MeV/c^2. However, the data are not conclusive, and the proximity of the $\bar{\Sigma}^*$ (1385) makes the signal difficult to interpret. Whatever the case, better statistics are needed to establish the $\bar{\Sigma}$ - $\bar{\Lambda}^{\circ}$ difference.

In conclusion, we see a large increase in charged anti-sigma production between $\sqrt{s}$ = 4 and 7 GeV which cannot be explained by simple inclusive particle production models. The amount of increase is consistent with naive charmed baryon predictions. However, the statistics are too poor to confirm such an

hypothesis without further corraborating evidence.

VII. CHARMED BARYON SEARCH

The theoretical mass spectrum[36,37] for the lowest lying nonstrange charmed baryons is depicted in Fig. 17. The $\bar{\Lambda}_c^-$ is searched for through its decay to $\bar{\Sigma}^{\pm}\pi^{\mp}\pi^-$. The other higher mass particles $\bar{\Sigma}_c^*$ and $\bar{\Sigma}_c$ can then be looked for in $\bar{\Sigma}^{\pm}\pi^{\mp}\pi^-\pi^{+,-}$ distributions where the $\bar{\Sigma}^{\pm}\pi^{\mp}\pi^-$ combination fits the $\bar{\Lambda}_c^-$ mass.

The mass resolution for the $\bar{\Lambda}_c^-$ and the higher mass states are found by a Monte Carlo technique similar to the one described in Sec. VI B for anti-sigmas. A $\bar{\Lambda}_c^-$ mass resolution of σ = 15-20 MeV is found, with the higher mass states being slightly larger. However, the resolution for the mass difference $\Delta M \equiv M_{\bar{\Sigma}3\pi} - M_{\bar{\Sigma}2\pi}$ is quite good (σ = 2-4 MeV) since it only depends on the momentum of the additional charged pion.

All anti-neutron candidates in the 7 GeV data which have an $\bar{n}\,\pi^{\pm}$ mass combination within 2σ (20 MeV) of the correct $\bar{\Sigma}^{\pm}$ mass are used for the charmed baryon search. This includes a total of 39 events of which 35 have at least two additional charged tracks.

To obtain the best $\bar{\Lambda}_c^-$ mass resolution, the anti-neutron momentum is constrained to give the correct $\bar{\Sigma}^{\pm}$ mass. Using this momentum and the remaining charged tracks, $\bar{\Sigma}^{\pm}\pi^{\mp}\pi^-$ mass combinations are formed. Figure 18 gives the plot for masses between 1.9 and 2.6 GeV/c^2. The events are numbered to show the multiple counting. Figure 18 also depicts these points in a scatter plot versus ΔM, the difference in mass between the $\bar{\Lambda}_c^-$ candidate and the mass formed by the addition of another pion. The expected intersection regions for $\bar{\Sigma}_c^*/\bar{\Sigma}_c$ decays[36,37] are shown by cross-hatching, where we have tried to account for the uncertainty in the particle's mass and width, as well as our resolution. The oval around each point gives the best estimate of the mass errors for that event. These are

found by smearing all the experimental parameters, including the pion momenta, and observing the change in the mass values.

There is one event (20) in the 2.24-2.28 GeV/c^2 region of the $M_{\bar{\Sigma}2\pi}$ plot which does not satisfy the $\bar{\Sigma}_c^*/\bar{\Sigma}_c$ decay scheme. This is to be compared with an expected background from side-bin populations of $\sim$ 1.1 events. There are three events (6, 10, 13), though, in the region 2.29-2.34 GeV/c^2, which do have combinations consistent with $\bar{\Sigma}^*_c$ decay. The background from side-bin populations would predict $\sim$ 0.3 events. However, this is $\sim$ 50 MeV/c^2 above the expected $\bar{\Lambda}_c^-$ mass and is probably a statistical fluctuation.

Using a detection efficiency for each additional pion of 0.7, one event would correspond to a $\sigma_{\bar{\Lambda}_c}$ x BR ($\rightarrow \bar{\Sigma}^{\pm}\pi^{\mp}\pi^-$) of 26 pb and a $R_{\bar{\Lambda}_c} \equiv \sigma_{\bar{\Lambda}_c}$ x BR ($\rightarrow \bar{\Sigma}^{\pm}\pi^{\mp}\pi^-$)/$\sigma_{\mu\mu}$ of $0.01\overline{4}$. Thus, we set an upper limit, at the 90% confidence level, of $\sigma_{\bar{\Lambda}_c}$ x BR ($\rightarrow \bar{\Sigma}^{\pm}\pi^{\mp}\pi^-$) < 56 pb and $R_{\bar{\Lambda}_c} < 0.03$.

If we assume that all the new production of $\bar{\Sigma}^{\pm}$'s given by Eq. (1) is due to charmed baryon decays, then we can estimate the expected value for $R_{\bar{\Lambda}_c}$ by:

$$R_{\bar{\Lambda}_c} \equiv \sigma_{\bar{\Lambda}_c} \times BR(\rightarrow \bar{\Sigma}^{\pm}\pi^{\mp}\pi^-)/\sigma_{\mu\mu}$$

$$= \Delta R_{\bar{\Sigma}} \times BR_{NL} \times f_{\bar{\Sigma}2\pi} \times f_{\pi^{\mp}\pi^-} \qquad (2)$$

where:

BR_{NL} is the percentage of $\bar{\Lambda}_c^-$ decays to $\bar{\Sigma}^{\pm}$'s which are nonleptonic (eliminating $\bar{\Sigma}\pi e^-\nu$, etc.),

$f_{\bar{\Sigma}2\pi}$ is the fraction of the nonleptonic decays which contain only two pions,

$f_{\pi^{\mp}\pi^-}$ is the fraction of those decays where both the pions are charged.

There are no direct experimental measurements of BR_{NL}. Theoretical predictions [38,39] place the $\bar{\Lambda}_c^-$ semileptonic branching ratio at anywhere from 10% to 40%. We will use 20% or in other words $BR_{NL} = 0.8$.

Using a version of the Fermi statistical model, Lee, Quigg, and Rosner[37] find a value of $f_{\bar{\Sigma}2\pi} = 0.3$. Rosner and Peshkin[40] calculate upper and lower limits for $f_{\pi^\mp\pi^-}$, from weak interaction isospin resistrictions, of

$$0.5 < f_{\pi^\mp\pi^-} < 0.8.$$

Taking an average value of 0.65 for this term, allows us to solve Eq. (2):

$$R_{\bar{\Lambda}_c} \simeq 0.12 \times 0.8 \times 0.3 \times 0.65 = 0.02.$$

One event in the $\bar{\Sigma}^\pm \pi^\mp\pi^-$ mass plot corresponds to an $R_{\bar{\Lambda}_c}$ value of 0.014. Thus, from the estimate of $\bar{\Lambda}_c^-$ production above, the expected number of events is ~ 1. The upper limit of $R_{\bar{\Lambda}_c} < 0.03$ is then entirely consistent with simple expectations for charmed baryon production.

Therefore, even though we see a large increase in inclusive charged anti-sigma production between $\sqrt{s}$ = 4 and 7 GeV, which is consistent with charmed baryon production, our sensitivity to the exclusive $\bar{\Sigma}^\pm \pi^\mp\pi^-$ is too small to observe a charmed baryon signal.

ACKNOWLEDGMENTS

This research was supported by the Department of Energy under contract number EY-76-C-03-0515. We wish to acknowledge the help of the entire SLAC-LBL collaboration and in particular that of A. Boyarski, V. Lüth and W. Tannenbaum. We would also like to thank F. Gilman for many useful discussions.

* Present address: University of Massachusetts, Amherst, Mass.

† Present address: Varian Associates, Palo Alto, Ca.

ǂ Present address: Institute de Physique Nucléaire, Orsay, France.

1. J. -E. Augustin et al., Phys. Rev. Lett. 33, 1406 (1974); J. J. Aubert et al., Phys. Rev. Lett. 33, 1404 (1974).
2. G. S. Abrams et al., Phys. Rev. Lett. 33, 1453 (1974).
3. G. Goldhaber et al., Phys. Rev. Lett. 37, 255 (1976).
4. I. Peruzzi et al., Phys. Rev. Lett. 37, 569 (1976).
5. G. Hanson et al., Phys. Rev. Lett. 35, 1609 (1975).
6. M. L. Perl et al., Phys. Rev. Lett. 35, 1489 (1975); M. L. Perl et al., Phys. Lett. 63B, 466 (1976).
7. R. F. Schwitters, Proc. 1975 Int. Symposium on Lepton-Photon Interactions at High Energies, Stanford, 1975.
8. S. D. Drell, D. J. Levy, and T. Yan, Phys. Rev. D 1, 1617 (1970).
9. Proposal SP-10.
10. J. -E. Augustin et al., Phys. Rev. Lett. 34, 233 (1975).
11. W. Tannenbaum et al., Phys. Rev. D 17, 1731 (1978).
12. I. Peruzzi et al., Phys. Rev. D 17, 2901 (1978).
13. T. Ferguson, et al., to be published in Phys. Lett. B.
14. A. Boyarski et al., Phys. Rev. Lett. 34, 764 (1975).
15. R. Hollebeck, thesis, Lawrence Berkeley Laboratory Publication No. LBL-3874, 1975.
16. J. Siegrist et al., Phys. Rev. Lett. 36, 700 (1975).
17. T. Coor et al., Phys Rev. 98, 1369 (1955).
18. B. Bracci et al., CERN/HERA 73-1, 1973 (unpublished).
19. H. -J. Besch et al., DESY Report No. DESY 77/28, 1977 (unpublished).
20. O. Chamberlain et al., Phys. Rev. 113, 1615 (1959).
21. L. E. Agnew et al., Phys. Rev. 118, 1371 (1960).
22. A. G. Ekspong et al., Nuc. Phys. 22, 353 (1961).

23. W. H. Barkas et al., Phys. Rev. 105, 1037 (1957).

24. C. C. Morehouse, Proceedings of Summer Institute on Particle Physics 1975, SLAC REPORT NO. 191, Nov. 1975.

25. M. Piccolo et al., Phys Rev. Lett. 39, 1503 (1977).

26. D. G. Aschman et al., Stanford Linear Accelerator Center Publication (SLAC-PUB-2128, 1978, submitted to Phys. Rev. Lett.).

27. J. Burmester et al., Phys. Lett. 67B, 367 (1977); V. Lüth et al., Phys. Lett. 70B, 120 (1977).

28. G. A. Sayer et al., Phys. Rev. 169, 1045 (1968); F. Uchiyama and J. Loos, Particle Data Group LBL-55, 1972 (unpublished); W. E. Cleland et al., Phys. Rev. D 12, 1247 (1975).

29. E. Bracci et al., CERN-HERA 72-2, 1972 (unpublished).

30. M. M. Sternheim and R. R. Silbar, Phys. Rev. D 6, 3117 (1972).

31. V. Lüth, Proceedings of the XII Rencontre de Moriond (Flaine, 1977), edited by Tran Thanh Van, R.M.I.E.M., Orsay.

32. G. J. Feldman and M. L. Perl, Phys. Rep. 19C, 233 (1975), Appendix B.

33. W. Braunschweig et al., Phys. Lett. 63B, 115 (1976).

34. R. Hagedorn, Nucl. Phys. B24, 93 (1970); E. L. Feinberg, Phys.Rep. 5C, 237 (1972).

35. A. De Rújula, H. Georgi, and S. L. Glashow, Phys. Rev. Lett. 37, 785 (1976).

36. A. De Rújula, H. Georgi, and S. L. Glashow, Phys. Rev. D 12, 147 (1975).

37. B. W. Lee, C. Quigg, and J. L. Rosner, Phys. Rev. D 15, 157 (1977).

38. M. K. Gaillard, B. W. Lee, and J. L. Rosner, Rev. Mod. Phys. 47, 277 (1975).

39. J. Ellis, M. K. Gaillard, and D. V. Nanopoulos, Nuc. Phys. B100, 313 (1975).

40. M. Peshkin and J. Rosner, Nuc. Phys. B122, 144 (1975).

TABLE I. Integrated luminosity and number of detected hadronic events.

$\sqrt{s}$ (GeV)	$\int L \cdot dt$ (pb^{-1})	# hadronic events
4	3.4	51,000
7	11.5	74,000
$\psi(3.1)$	.23	91,000

TABLE II. Cosmic ray background subtractions.

$\sqrt{s}$ (GeV)	4	7	$\psi(3.1)$
Using T Counters			
# with TOF < 4ns	78	59	14
# with TOF < 4ns, Passing $\bar{n}$ Cuts	1	3	0
# with TOF > 6ns	250	149	63
Estimated Background	6.5 ± 3.3	3.9 ± 2.0	1.6 ± 0.8
Using A Counters			
# with TOF < 6ns	108	77	31
# with TOF < 6ns Passing $\bar{n}$ Cuts	4	5	3
# with TOF > 10ns	175	134	60
Estimated Background	9.2 ± 2.7	7.1 ± 2.0	3.2 ± 0.9

TABLE III. K_L^o background subtractions.

$\sqrt{s}$ (GeV)	4	7	$\psi(3.1)$
# of K_L^o's Aimed At $\bar{n}$ Packages	1400 ± 100	1800 ± 370	1900 ± 200
# of K_L^o's Passing $\bar{n}$ Cuts	34 ± 14	47 ± 21	46 ± 20

TABLE IV. Photon background subtractions.

$\sqrt{s}$ (GeV)	4	7	ψ(3.1)
# Hadronic Events	51,000	74,000	91,000
$\langle n_\gamma \rangle$	4	4.5	3.5
# γ's Hitting $\bar{n}$ Packages	22,000	37,000	35,000
Estimated Background	3.0 ± 1.5	4.8 ± 2.4	4.5 ± 2.3

TABLE V. Summary of all background subtractions and the final number of anti-neutron events.

$\sqrt{s}$ (GeV)	4	7	ψ(3.1)
#$\bar{n}$ Candidates	100	150	164
Cosmic Background	15.7 ± 4.2	11.0 ± 2.8	4.8 ± 1.2
K_L° Background	34 ± 14	47 ± 21	46 ± 20
Photon Background	3.0 ± 1.5	4.8 ± 2.4	4.5 ± 2.3
Neutron Background	6.2 ± 3.0	11.3 ± 4.7	14.1 ± 5.3
Final #$\bar{n}$ Events	41 ± 16	77 ± 21	95 ± 21

TABLE VI. The average multiplicity, momentum, total momentum, and total energy for charged particles in all hadronic events and ones with $\bar{n}$ candidates. The triggering efficiencies are taken from Ref. 32.

$\sqrt{s}$ (GeV)	4		7		$\psi(3.1)$	
	all	with $\bar{n}$	all	with $\bar{n}$	all	with $\bar{n}$
$\langle n^{\pm} \rangle$	3.93	3.76	4.68	4.46	3.60	2.84
$\langle p^{\pm} \rangle$(GeV/c)	0.51	0.47	0.64	0.58	0.47	0.46
$\langle p_{\pm tot} \rangle$(GeV/c)	2.02	1.54	3.03	2.56	1.69	1.30
$\langle E_{\pm tot} \rangle$(GeV)	2.23	1.76	3.31	2.83	1.85	1.52
$\langle \epsilon_{trig} \rangle$	0.55	0.5 ± 0.1	0.65	0.6 ± 0.12	0.45	0.4 ± 0.08

TABLE VII. The anti-neutron results showing the fraction of events which contain an $\bar{n}$ ($f_{\bar{n}}$), the total $\bar{n}$ cross section ($\sigma_{\bar{n}}$), and $R_{\bar{n}}$ ($\sigma_{\bar{n}}/\sigma_{\mu\mu}$).

$\sqrt{s}$ (GeV)	4	7	$\psi(3.1)$
$f_{\bar{n}}$	0.05 ± 0.024	0.068 ± 0.027	0.067 ± 0.024
$\sigma_{\bar{n}}$(nb)	1.35 ± 0.65	0.68 ± 0.27	59 ± 21
$R_{\bar{n}}$	0.28 ± 0.13	0.36 ± 0.14	6.5 ± 2.3

TABLE VIII. The $\bar{\Sigma}^{\pm}$ fitting parameters.

$\sqrt{s}$ (GeV)	4	7	$\psi(3.1)$
offset (MeV)	-6.6 ± 3.3	-6.6 ± 3.3	-3.7 ± 2.9
σ (MeV)	9.8 ± 3.4	9.8 ± 3.4	6.2 ± 2.8
χ^2/DOF	80/89	80/89	126/89
# $\bar{\Sigma}^{\pm}$'s	2.7 ± 3.8	26.4 ± 7.3	13.8 ± 5.2

TABLE IX. The $\bar{\Sigma}^{\pm}$ results giving the fraction of hadronic events containing an $\bar{\Sigma}^{\pm}$ ($f_{\bar{\Sigma}}$), the total $\bar{\Sigma}^{\pm}$ cross section ($\sigma_{\bar{\Sigma}}$), and $R_{\bar{\Sigma}}$ ($\sigma_{\bar{\Sigma}}/\sigma_{\mu\mu}$).

$\sqrt{s}$ (GeV)	4	7	ψ(3.1)
$f_{\bar{\Sigma}}$	0.004 ± 0.005	0.027 ± 0.007	0.010 ± 0.004
$\sigma_{\bar{\Sigma}}$(nb)	0.11 ± 0.14	0.26 ± 0.07	9.1 ± 3.4
$R_{\bar{\Sigma}}$	0.023 ± 0.029	0.14 ± 0.04	1.0 ± 0.4

Fig. 1 The Mark I magnetic detector. The proportional chambers are not shown.

Fig. 2 Enlargement of one anti-neutron package on the side of the Mark I.

Fig. 3 Difference in the x-y and x-z views between the positions of magnetic detector tracks and $\bar{n}$ chamber tracks extrapolated to the magnet radius (r=1.65 m).

Fig. 4 Computer reconstructed picture of a good anti-neutron event. The $\bar{n}$ emerges to the right and annihilates in the shower counter sending two forward prongs into the $\bar{n}$ package. One prong strikes an A counter giving a time approximately 7 nsec past prompt.

Fig. 5 Anti-neutron momentum distributions for the three center of mass energies uncorrected for background or efficiency.

Fig. 6 The Monte Carlo predicted anti-neutron detection efficiency as a function of the $\bar{n}$ momentum. The efficiency for the three detection possibilities are shown combined and separately.

Fig. 7 The number of protons and anti-protons identified by the Mark I time of flight system as a function of the scattering angle of prongs produced by them in the $\bar{n}$ packages. Also shown is the Monte Carlo predictions.

Fig. 8 $R_{\bar{n}}$ $(\sigma_{\bar{n}}/\sigma_{\mu\mu})$ and $R_{\bar{p}}$ $(\sigma_{\bar{p}}/\sigma_{\mu\mu})$ vs. $\sqrt{s}$.

Fig. 9 Anti-neutron and anti-proton differential momentum spectra for the three center of mass energies.

Fig. 10 The anti-baryon invariant cross sections for $\sqrt{s}$ = 7 GeV. The function is a fit to lower momentum pion data from Ref. 24.

Fig. 11 Anti-sigma mass distributions. Relative spectra are produced by subtracting the correct $\bar{\Sigma}^{\pm}$ mass from each $\bar{n}\,\pi^{\pm}$ combination.

Fig. 12 Separate $\bar{n}\,\pi^{+}$ and $\bar{n}\,\pi^{-}$ mass distributions for $\sqrt{s}$ = 7 GeV.

Fig. 13 Monte Carlo predicted anti-sigma mass resolution for four separate momentum ranges.

Fig. 14 $R_{\bar{\Sigma}}$ $(\sigma_{\bar{\Sigma}}/\sigma_{\mu\mu})$ and $R_{\bar{\Lambda}}{}^{\circ}$ $(\sigma_{\bar{\Lambda}}{}^{\circ}/\sigma_{\mu\mu})$ vs. $\sqrt{s}$.

Fig. 15 Anti-sigma momentum distribution for $\sqrt{s}$ = 7 GeV.

Fig. 16 $\bar{\Sigma}^{\pm}\pi^{\mp}$ mass distribution for $\sqrt{s}$ = 7 GeV data.

Fig. 17 Theoretical mass spectrum for the lowest mass charmed anti-baryons.

Fig. 18 $\bar{\Sigma}^{\pm}\pi^{\mp}\pi^{-}$ mass combinations between 1.9 and 2.6 GeV/c^2 listed by event number. The scatter plot shows these combinations plotted against $\Delta M = M_{\bar{\Sigma}3\pi} - M_{\bar{\Sigma}2\pi}$. The expected regions for charmed baryons are cross-hatched.

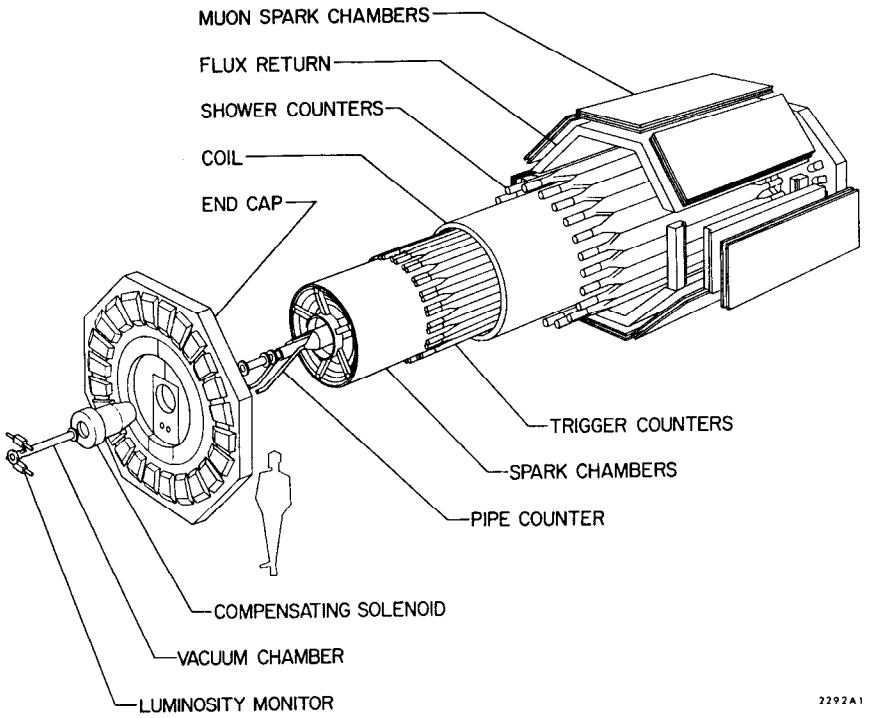
MUON SPARK CHAMBERS
FLUX RETURN
SHOWER COUNTERS
COIL
END CAP
TRIGGER COUNTERS
SPARK CHAMBERS
PIPE COUNTER
COMPENSATING SOLENOID
VACUUM CHAMBER
LUMINOSITY MONITOR
2292A1

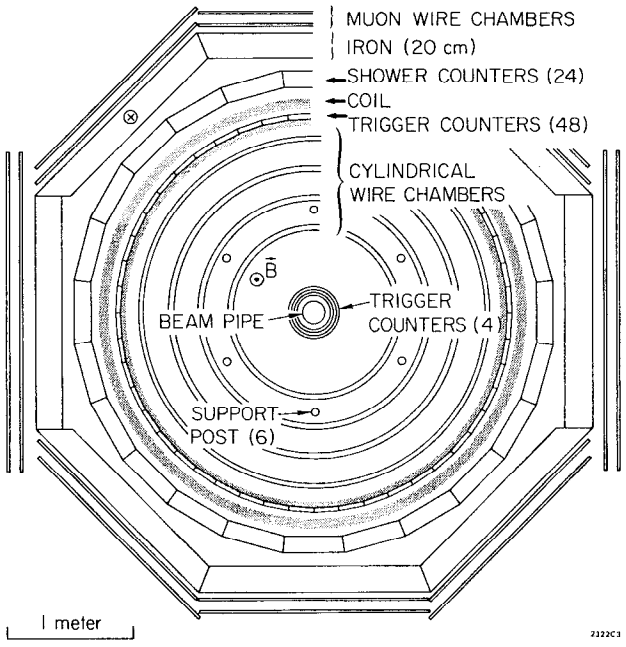
MUON WIRE CHAMBERS
IRON (20 cm)
SHOWER COUNTERS (24)
COIL
TRIGGER COUNTERS (48)
CYLINDRICAL
WIRE CHAMBERS
B
BEAM PIPE
TRIGGER
COUNTERS (4)
SUPPORT
POST (6)
1 meter
2122C3

Fig. 1

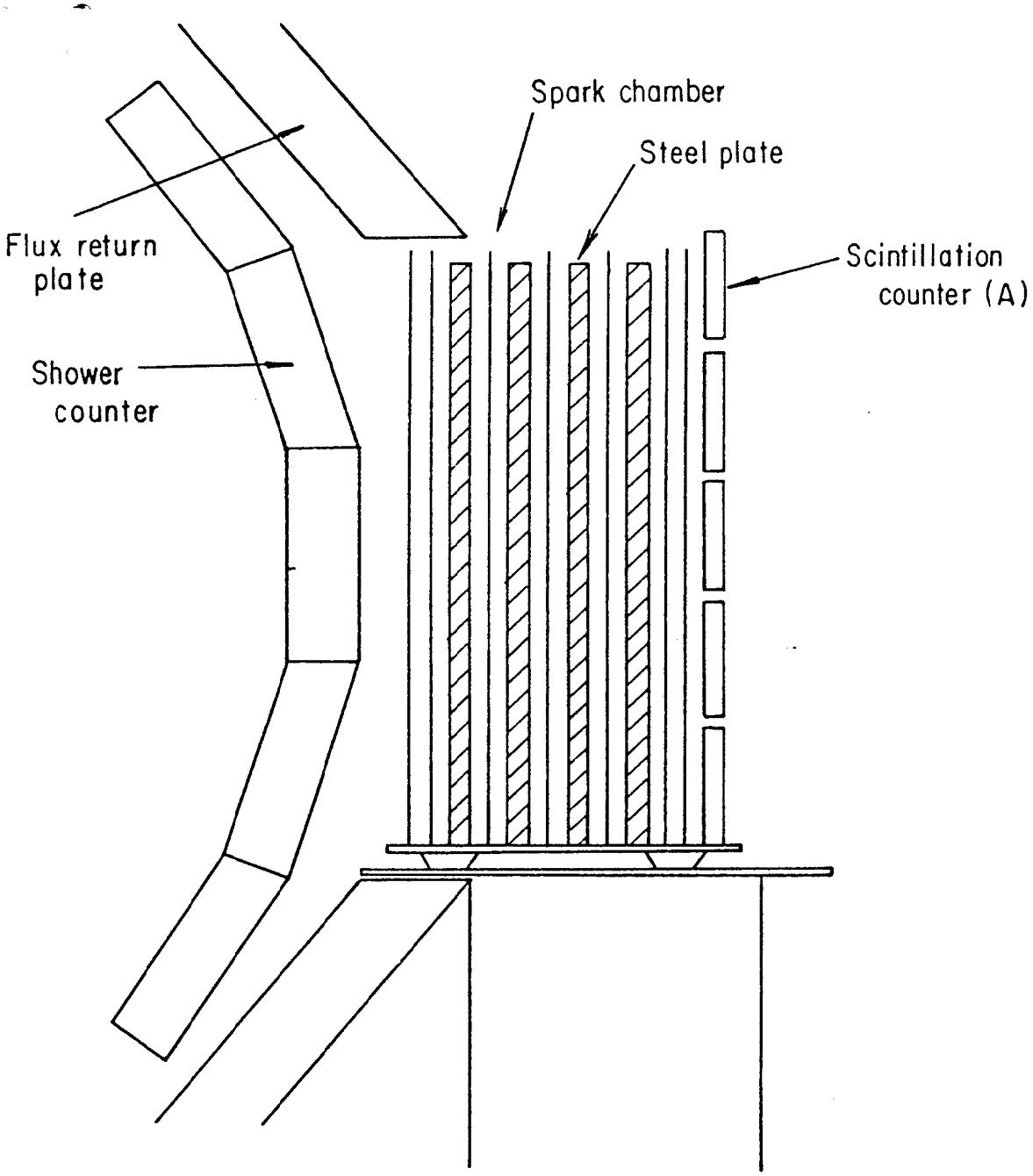
Spark chamber
Steel plate
Flux return plate
Scintillation counter (A)
Shower counter

Fig. 2

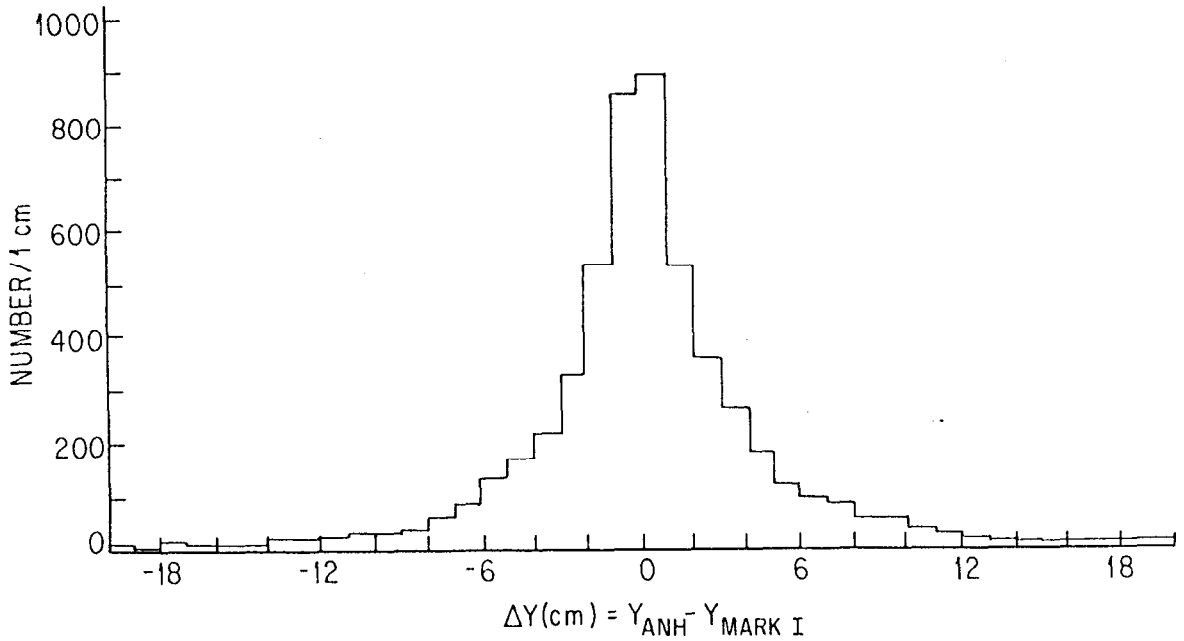
1000
800
600
400
200
0
NUMBER/1 cm
-18
-12
-6
0
6
12
18
ΔY(cm) = Y_ANH - Y_MARK I

Fig. 3A

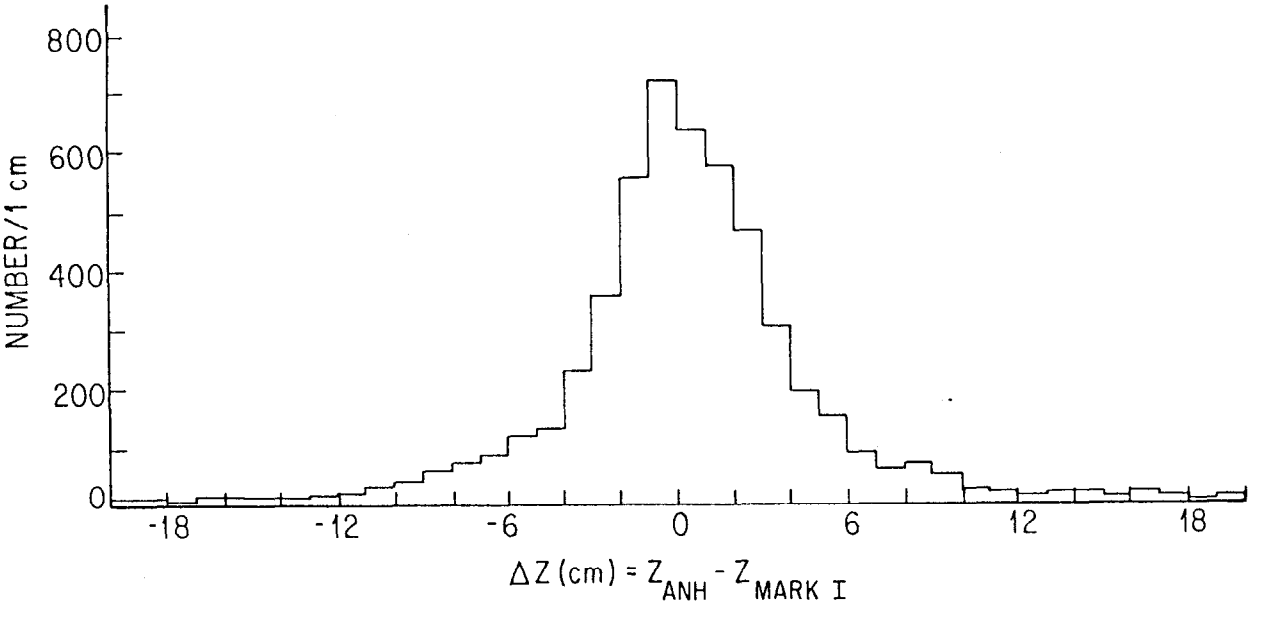

Fig. 3B

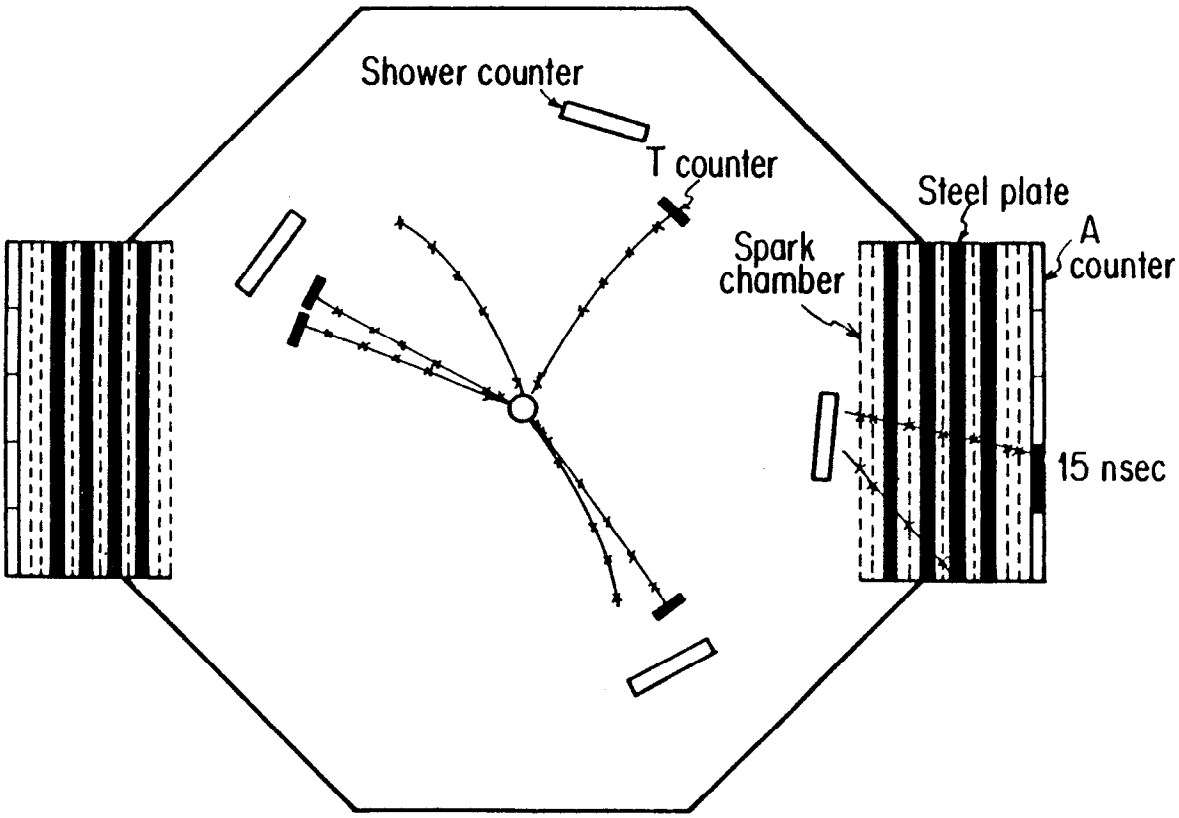
Shower counter
T counter
Steel plate
A
counter
Spark
chamber
15 nsec

Fig. 4

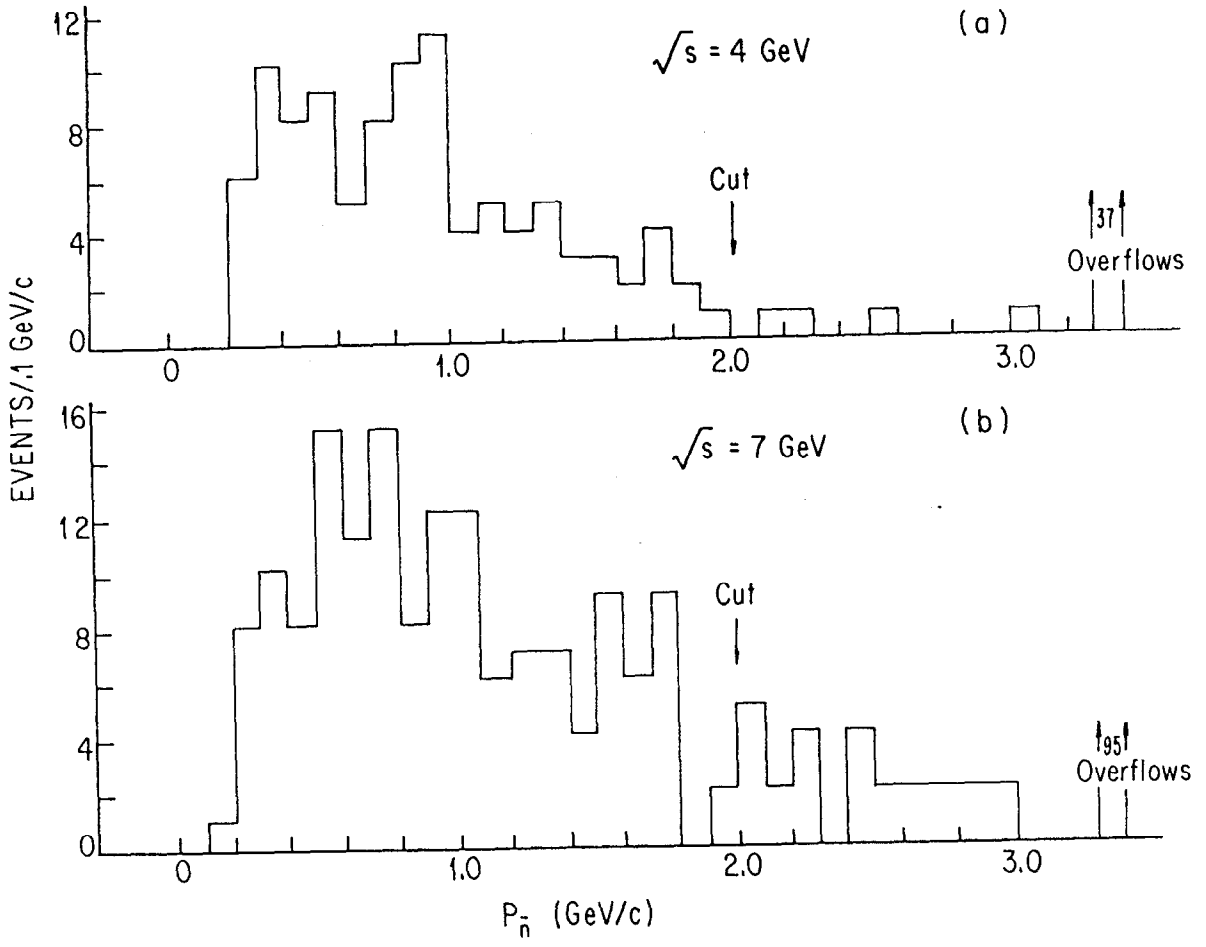
(a)
$\sqrt{s}$ = 4 GeV
Cut
37
Overflows
12
8
4
0
0
1.0
2.0
3.0
(b)
$\sqrt{s}$ = 7 GeV
Cut
95
Overflows
16
12
8
4
0
0
1.0
2.0
3.0
EVENTS/.1 GeV/c
$P_{\bar{n}}$ (GeV/c)

Fig. 5

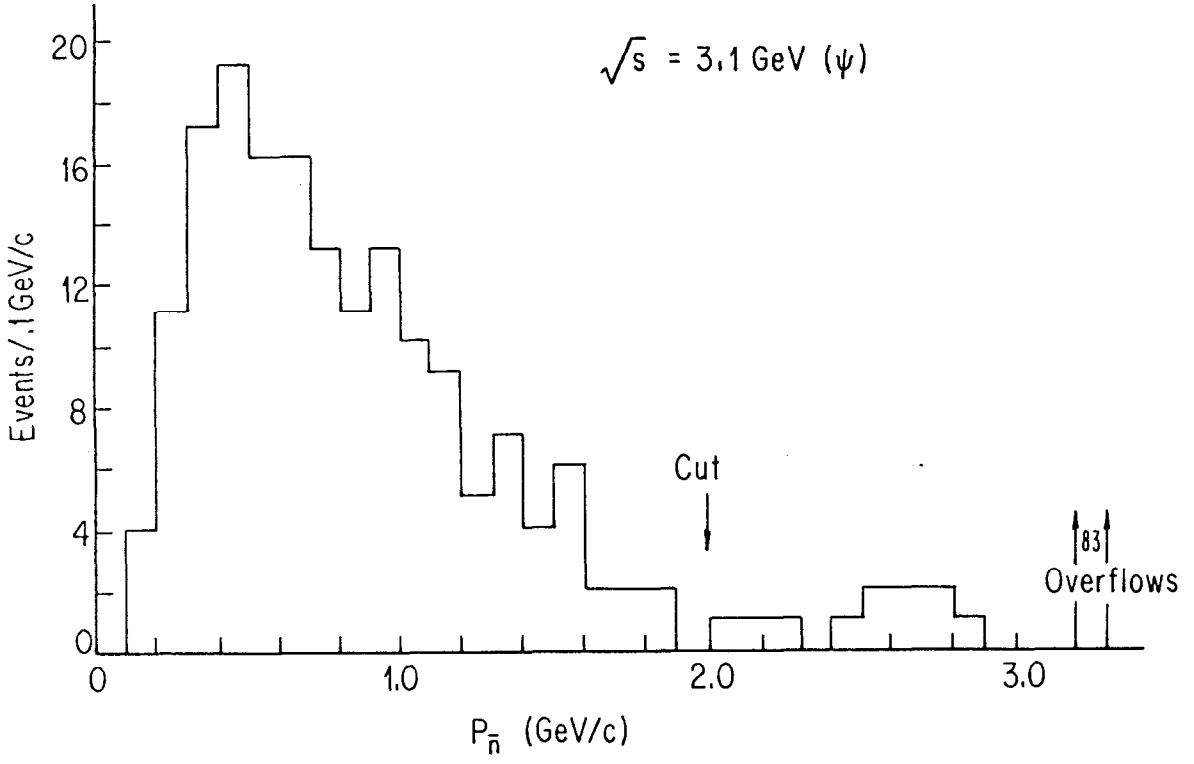
$\sqrt{s}$ = 3.1 GeV (ψ)
Events/.1GeV/c
20
16
12
8
4
0
0
1.0
2.0
3.0
Cut
83
Overflows
$P_{\bar{n}}$ (GeV/c)

Fig. 5c

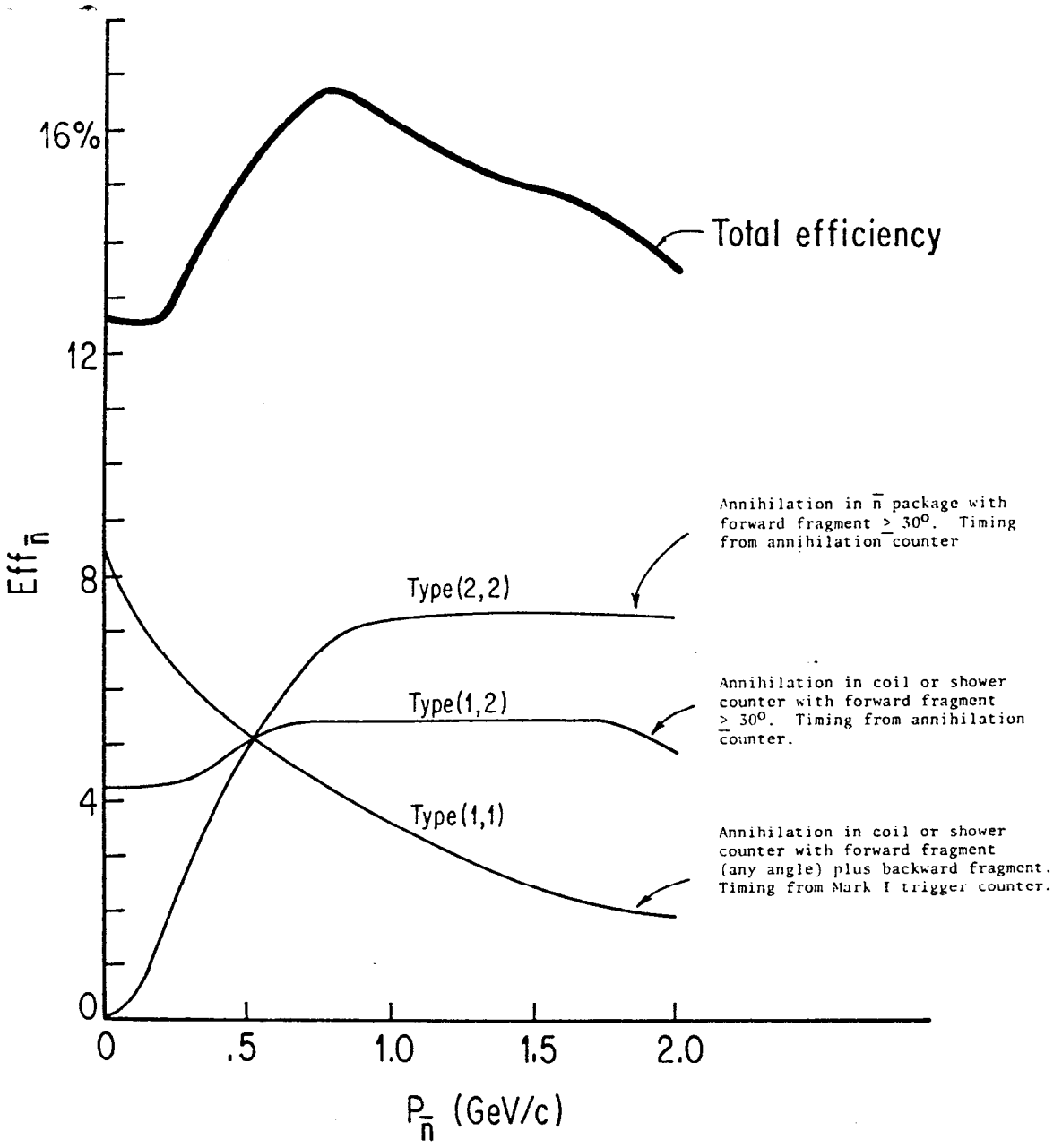
16%
12
8
4
0
$Eff_{\bar{n}}$
Total efficiency
Type(2,2)
Type(1,2)
Type(1,1)
Annihilation in $\bar{n}$ package with forward fragment $\geq 30^{o}$. Timing from annihilation counter
Annihilation in coil or shower counter with forward fragment $\geq 30^{o}$. Timing from annihilation counter.
Annihilation in coil or shower counter with forward fragment (any angle) plus backward fragment. Timing from Mark I trigger counter.
0
.5
1.0
1.5
2.0
$P_{\bar{n}}$ (GeV/c)

Fig. 6

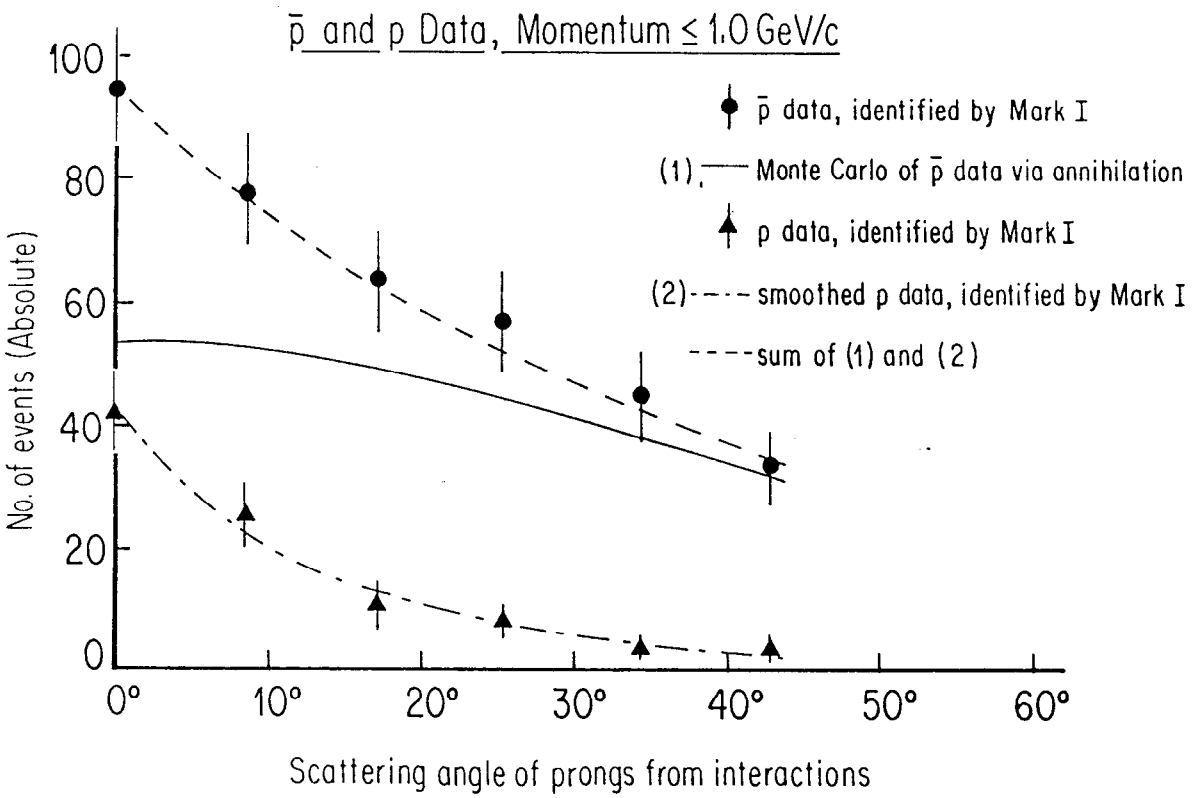
$\bar{p}$ and p Data, Momentum ≤ 1.0 GeV/c
$\bar{p}$ data, identified by Mark I
(1) Monte Carlo of $\bar{p}$ data via annihilation
p data, identified by Mark I
(2) smoothed p data, identified by Mark I
sum of (1) and (2)
No. of events (Absolute)
100
80
60
40
20
0
0°
10°
20°
30°
40°
50°
60°
Scattering angle of prongs from interactions

Fig. 7

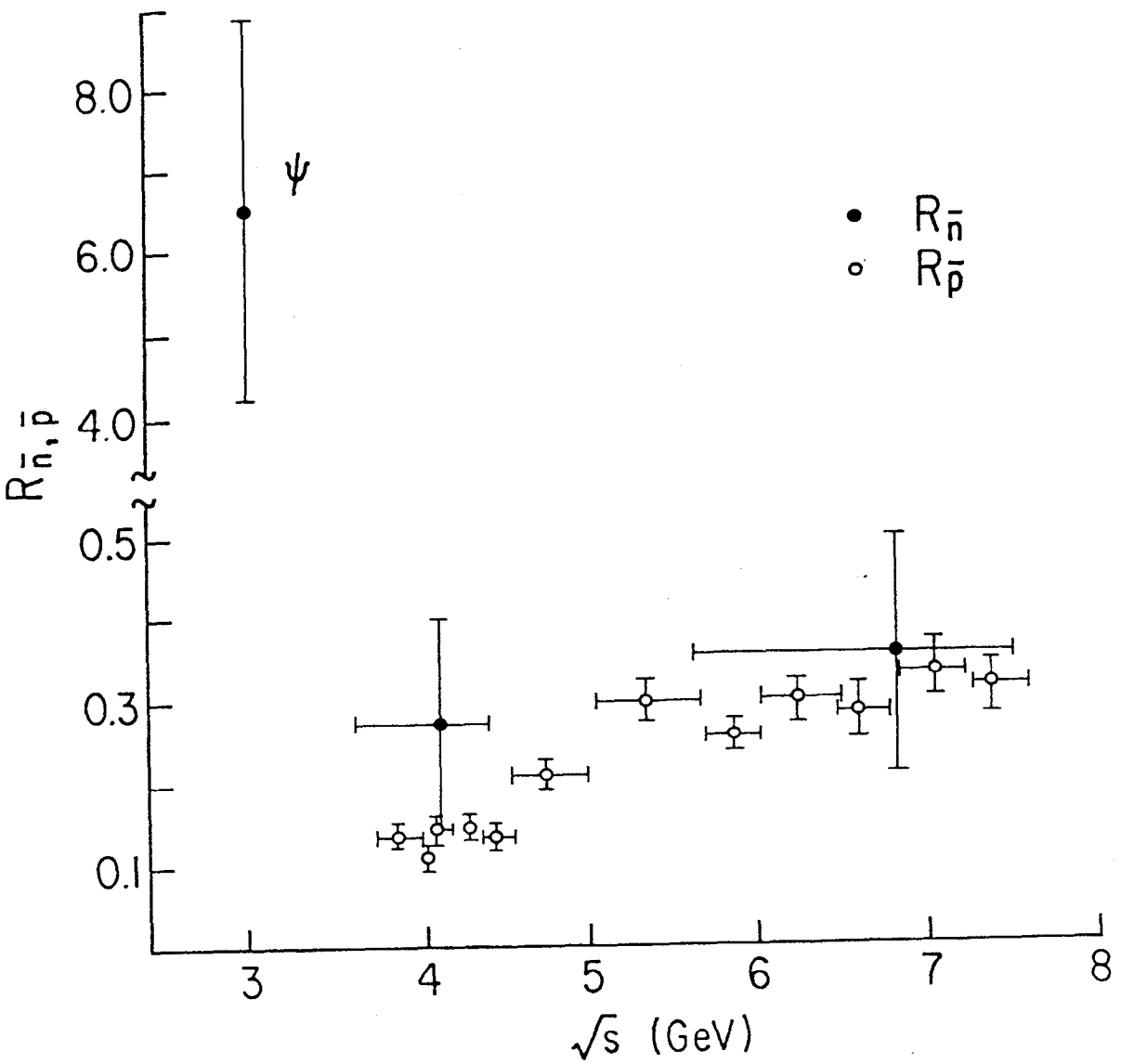

Fig. 8

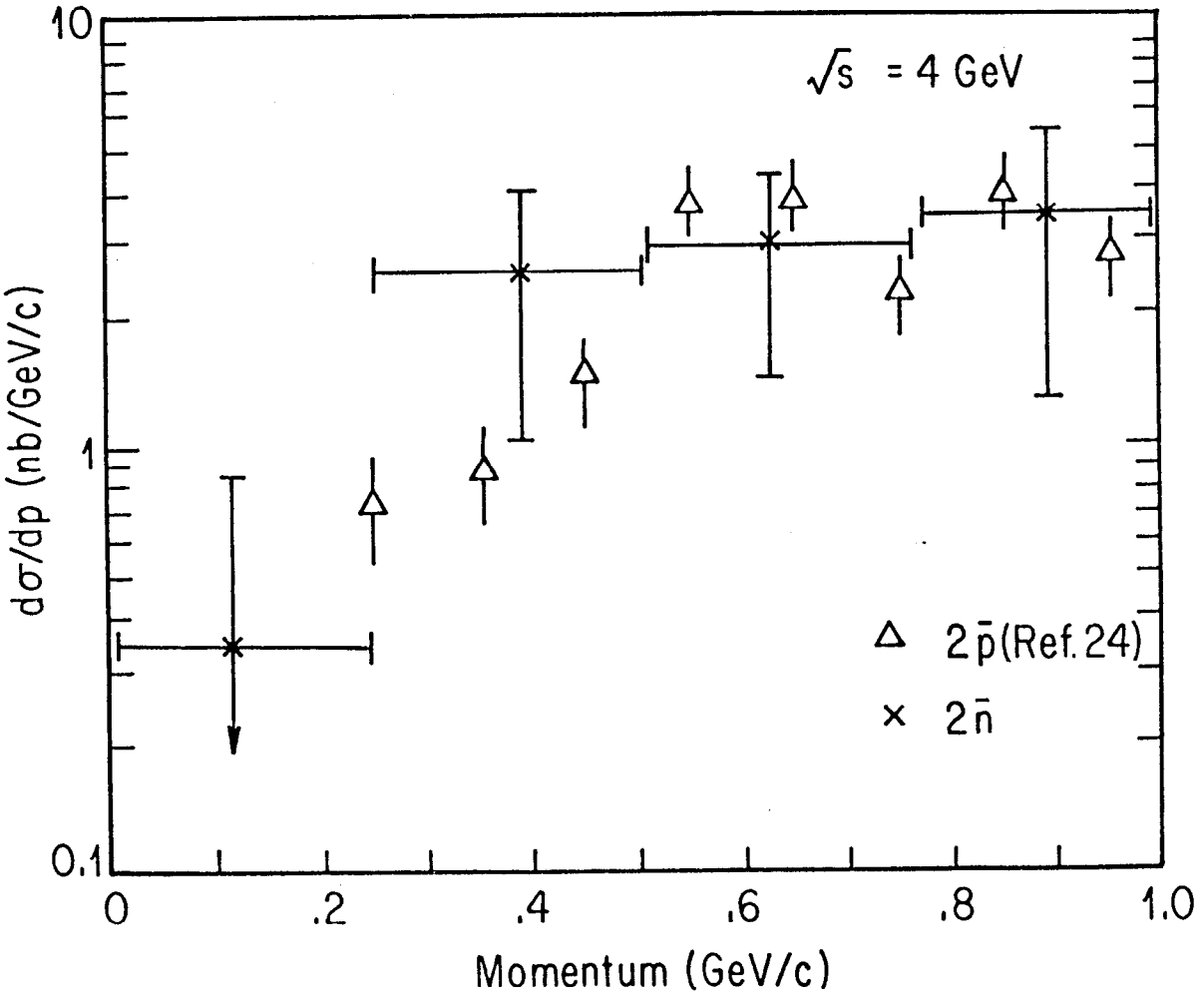
10
1
0.1
$\sqrt{s}$ = 4 GeV
dσ/dp (nb/GeV/c)
Δ 2p̄(Ref.24)
× 2n̄
0
.2
.4
.6
.8
1.0
Momentum (GeV/c)

Fig. 9A

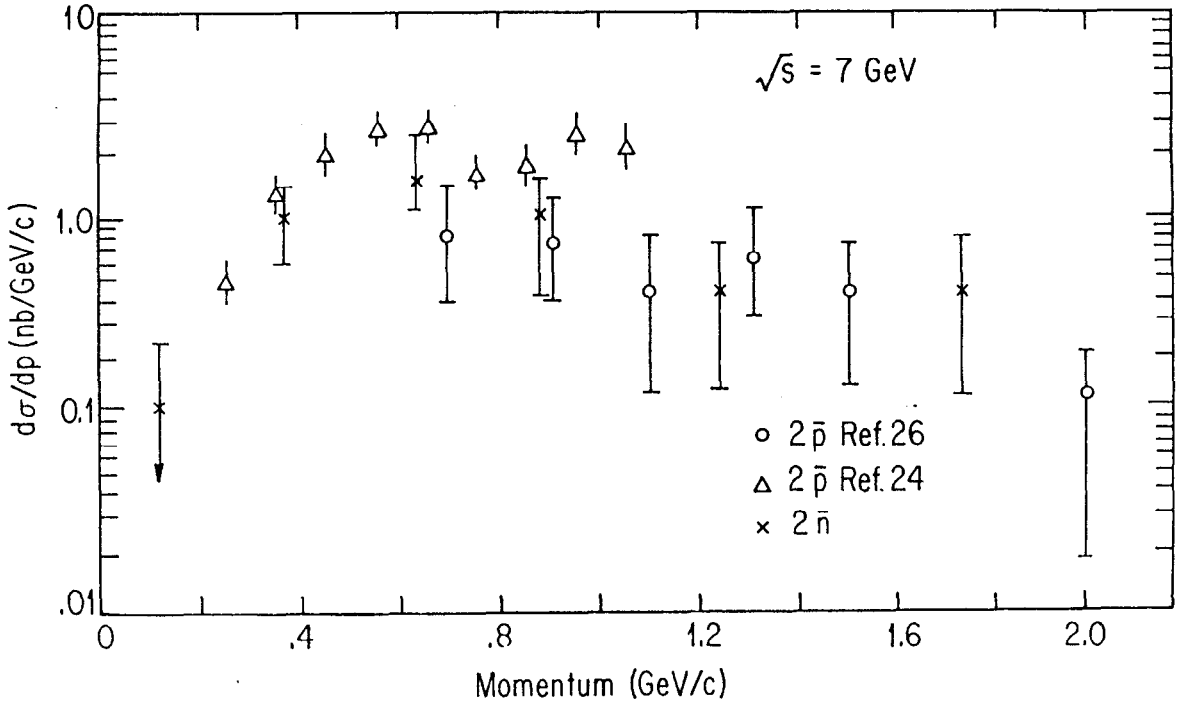
10
1.0
0.1
.01
dσ/dp (nb/GeV/c)
√s = 7 GeV
o 2p̄ Ref.26
△ 2p̄ Ref.24
× 2n̄
0
.4
.8
1.2
1.6
2.0
Momentum (GeV/c)

Fig. 9B

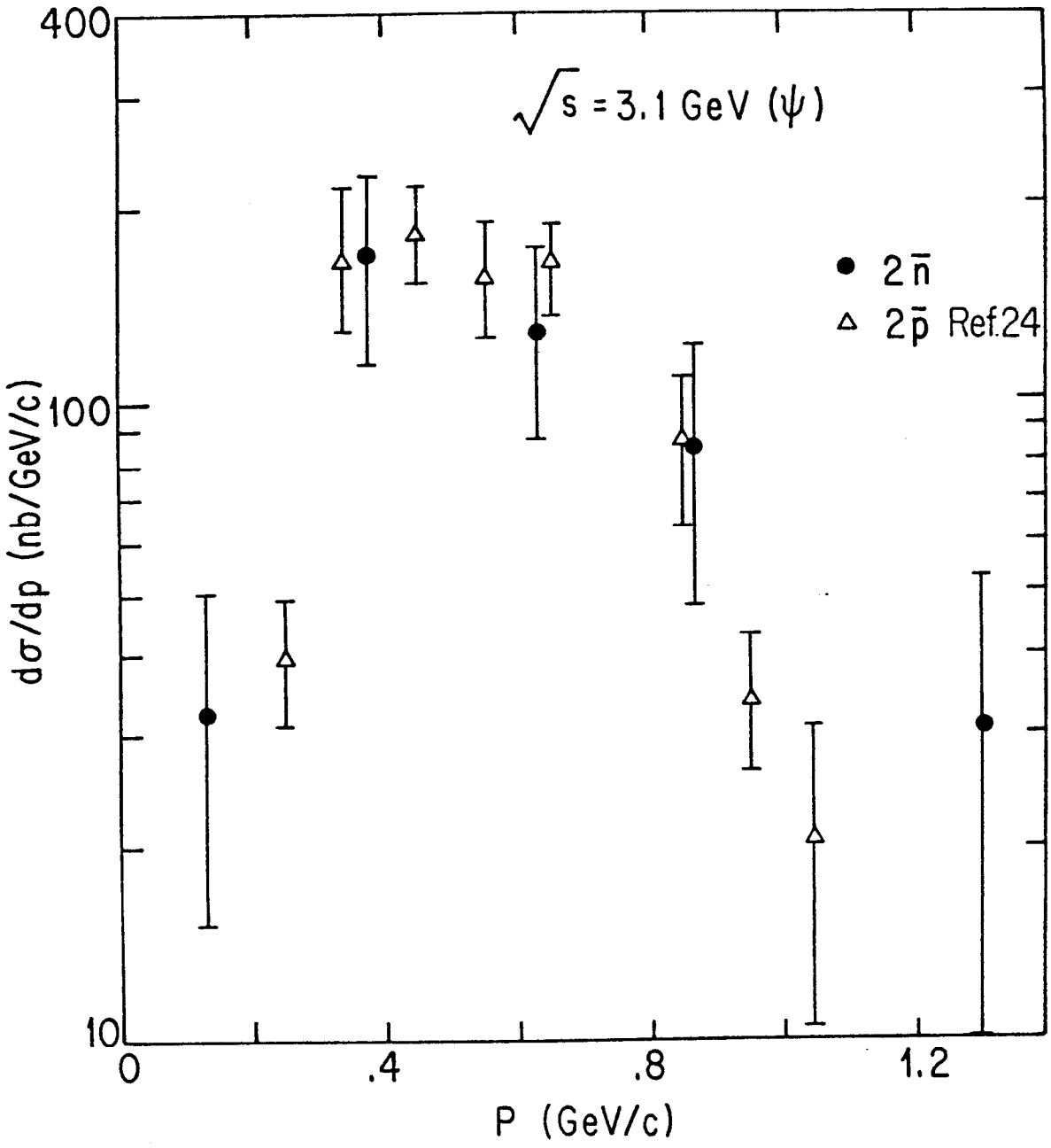
400
100
10
$\sqrt{s}$ = 3.1 GeV (ψ)
$2\bar{n}$
$2\bar{p}$ Ref.24
dσ/dp (nb/GeV/c)
0
.4
.8
1.2
P (GeV/c)

Fig. 9c

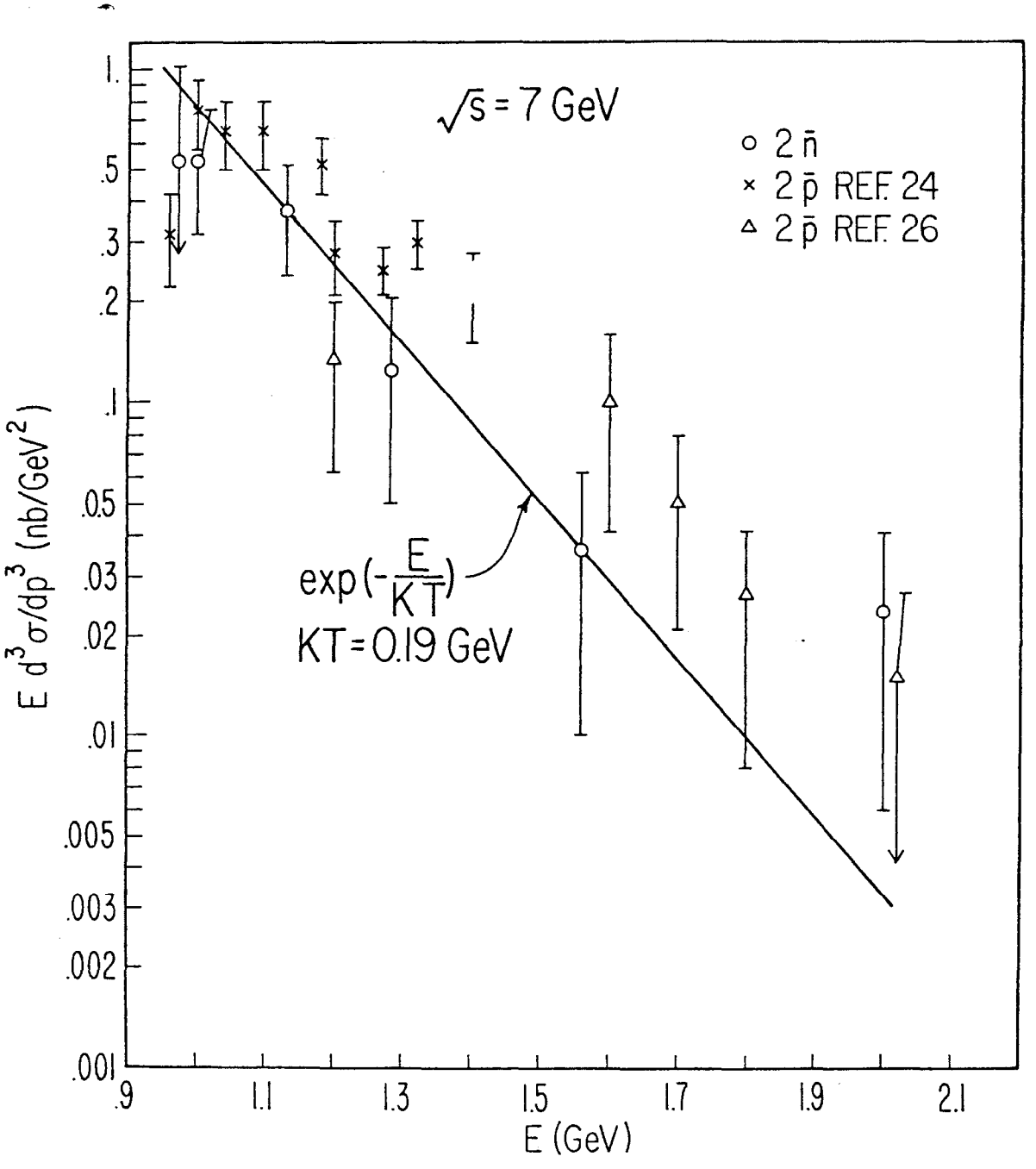
√s = 7 GeV
o 2 n̄
× 2 p̄ REF. 24
△ 2 p̄ REF. 26
exp(-E/KT)
KT = 0.19 GeV
E d³σ/dp³ (nb/GeV²)
E (GeV)
1.
.5
.3
.2
.1
.05
.03
.02
.01
.005
.003
.002
.001
.9
1.1
1.3
1.5
1.7
1.9
2.1

Fig. 10

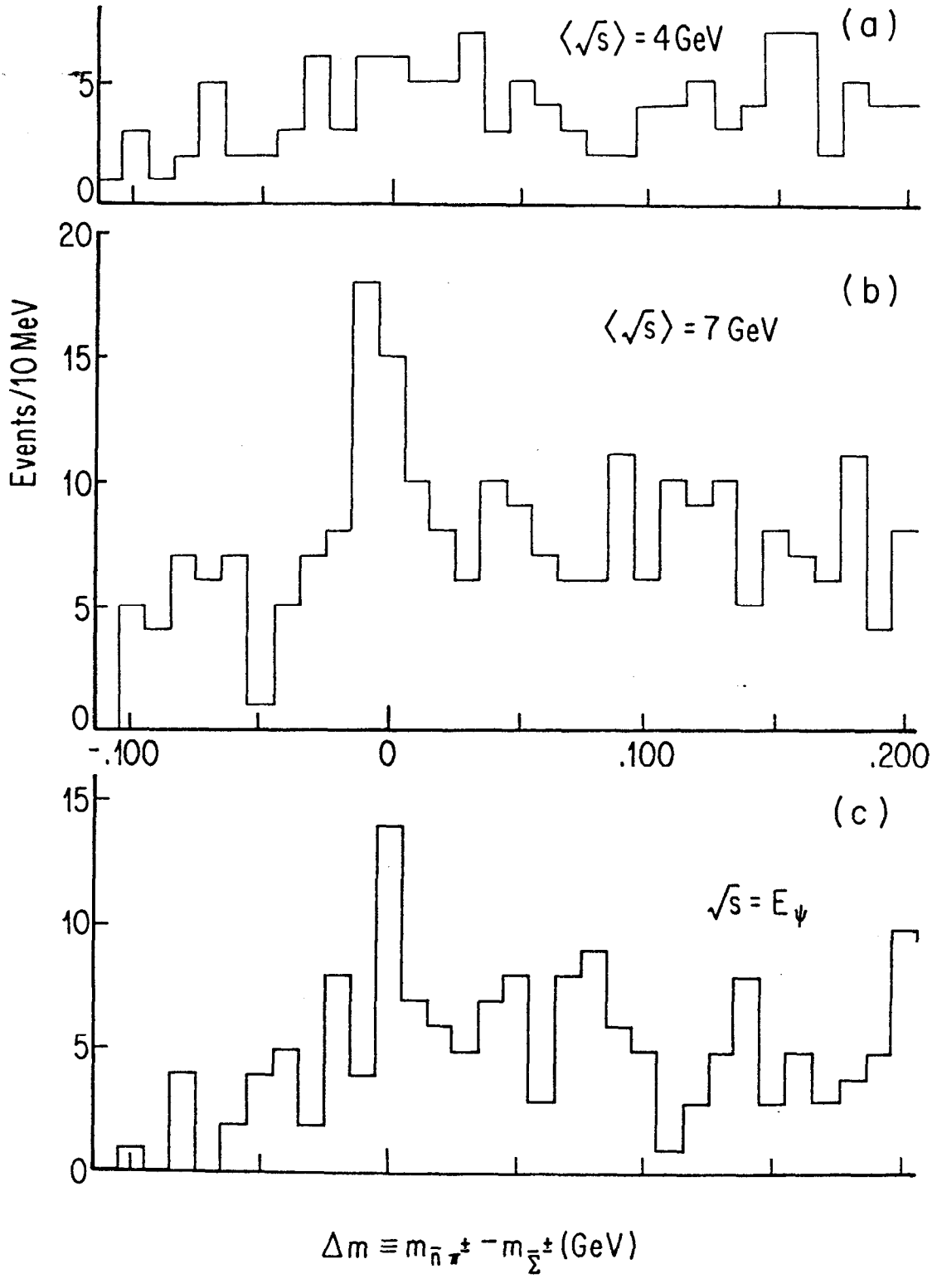
⟨√s⟩ = 4 GeV
(a)
5
0
20
(b)
⟨√s⟩ = 7 GeV
15
10
5
0
Events/10 MeV
-.100
0
.100
.200
15
(c)
√s = E_ψ
10
5
0
Δm ≡ m_{n̄π±} − m_{Σ̄±} (GeV)

Fig. 11

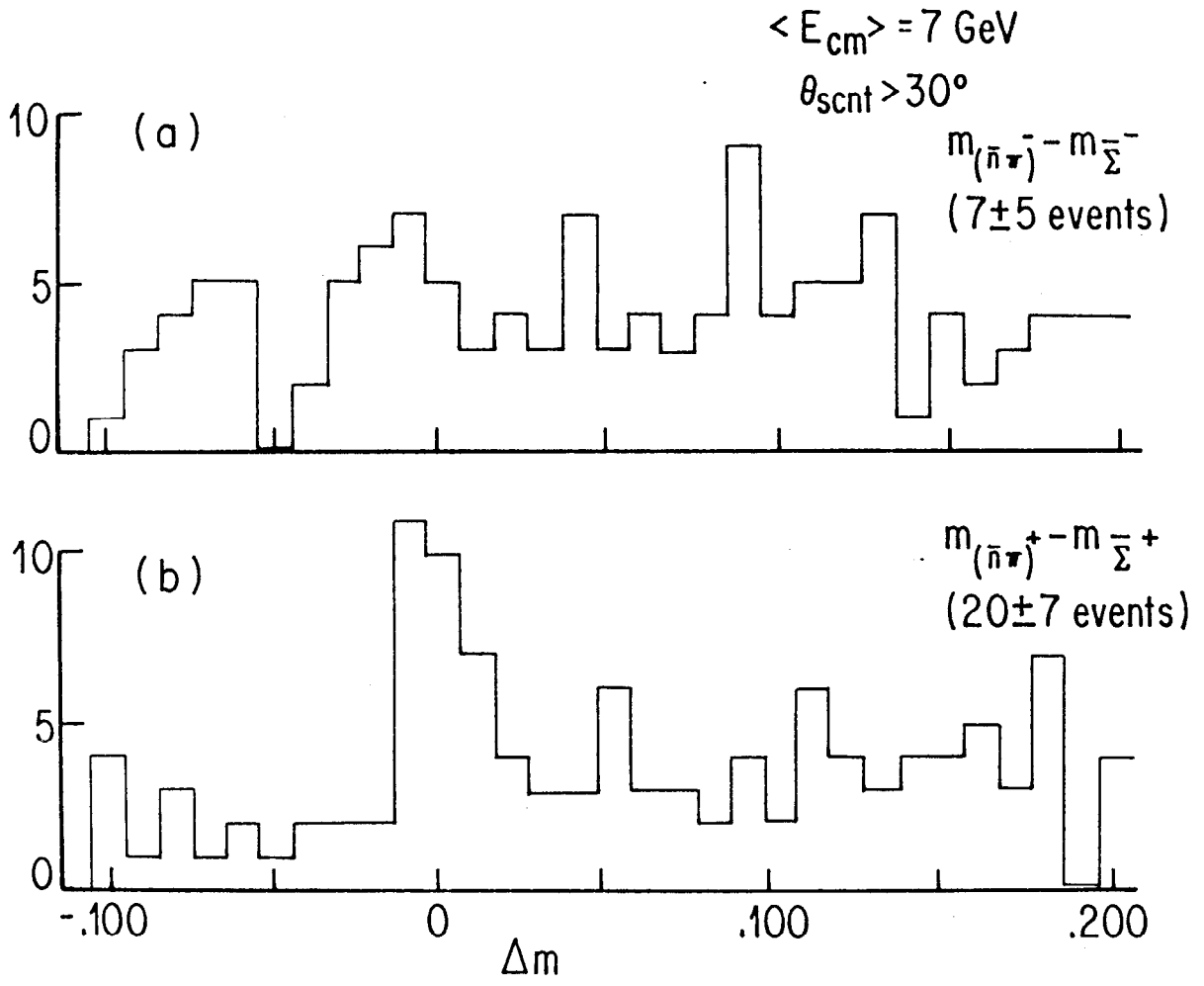
$\langle E_{cm} \rangle = 7$ GeV
$\theta_{scnt} > 30°$
(a)
$m_{(\bar{n}\pi^-)} - m_{\bar{\Sigma}^-}$
(7±5 events)
10
5
0
(b)
$m_{(\bar{n}\pi^+)} - m_{\bar{\Sigma}^+}$
(20±7 events)
10
5
0
-.100
0
.100
.200
Δm

Fig. 12

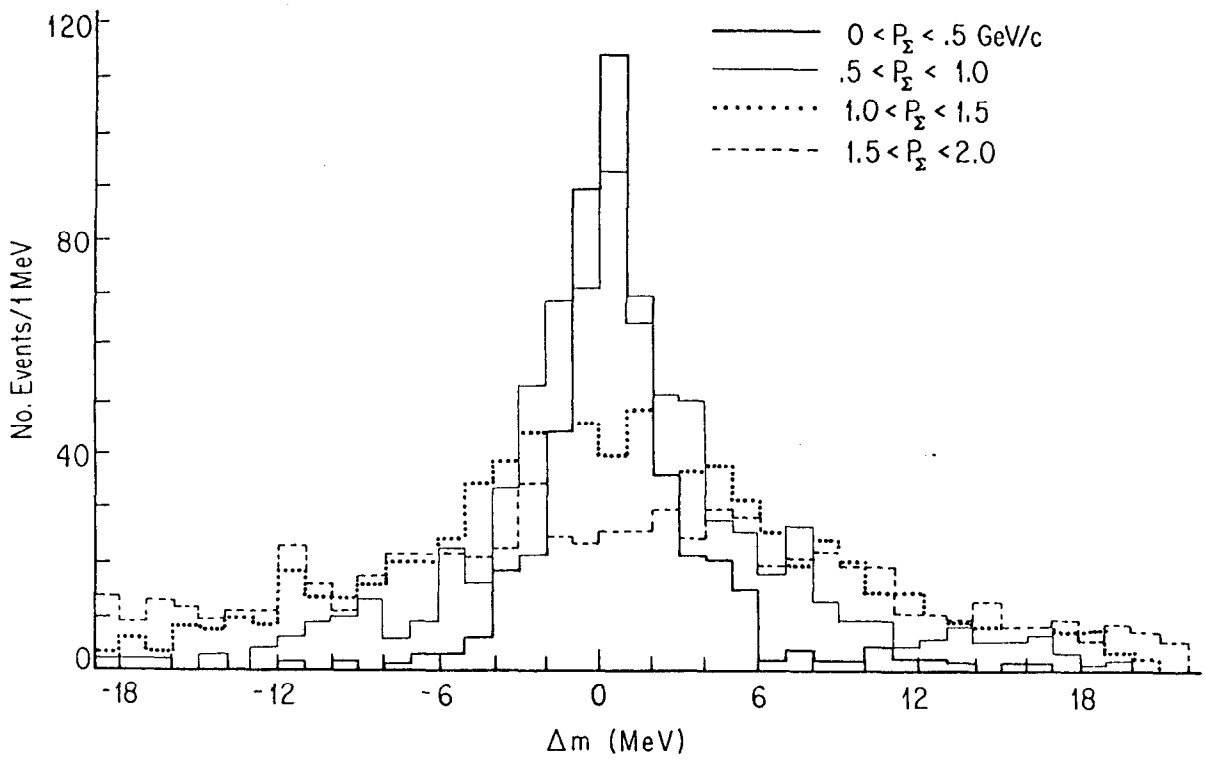
120
80
40
0
No. Events/1 MeV
-18
-12
-6
0
6
12
18
Δm (MeV)
0 < P_Σ < .5 GeV/c
.5 < P_Σ < 1.0
1.0 < P_Σ < 1.5
1.5 < P_Σ < 2.0

Fig. 13

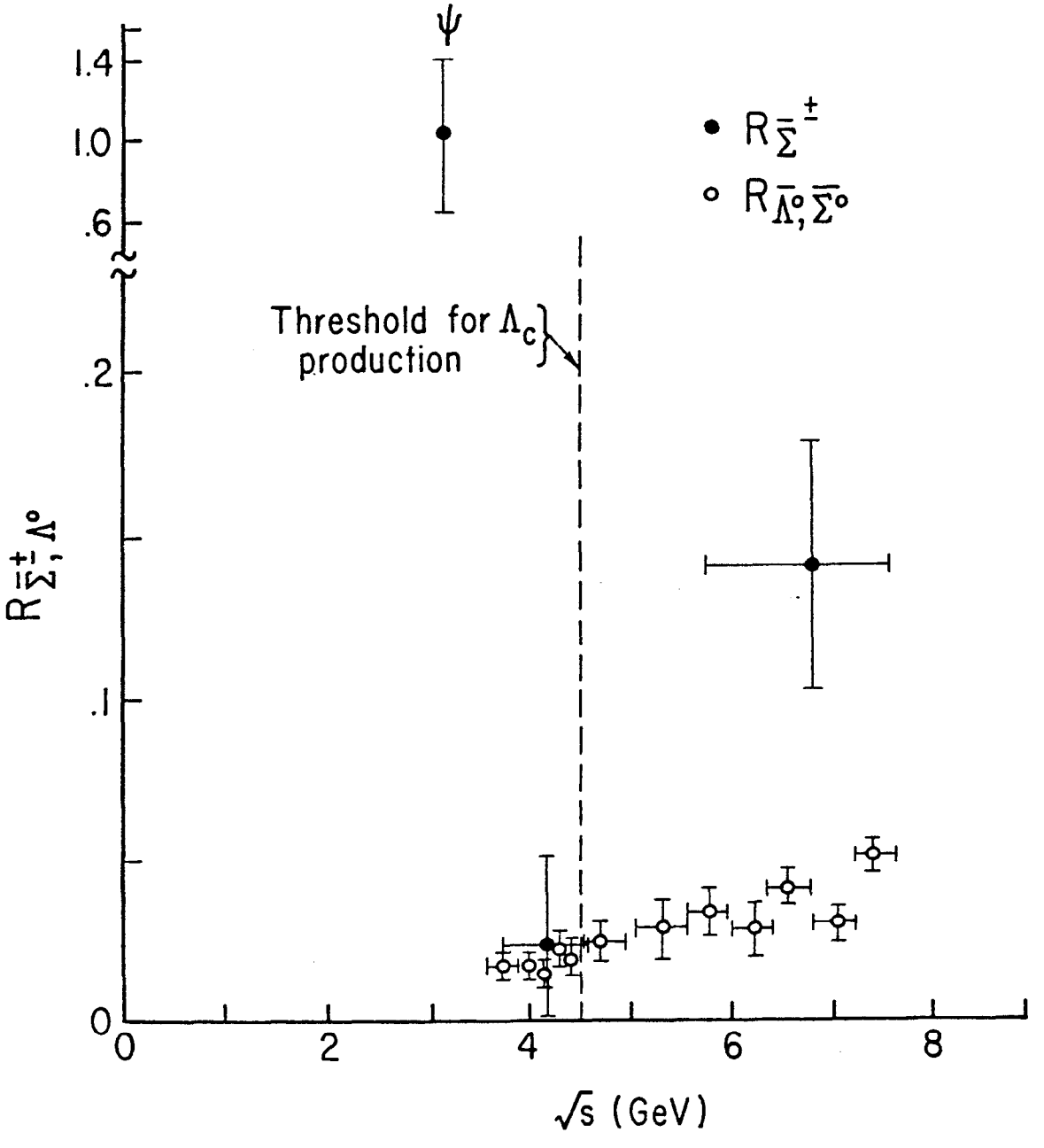
ψ
1.4
1.0
.6
.2
.1
0
$R_{\bar{\Sigma}^{\pm}}$
$R_{\bar{\Lambda}^0,\bar{\Sigma}^0}$
Threshold for Λ_c production
$R_{\bar{\Sigma}^{\pm},\Lambda^0}$
0
2
4
6
8
$\sqrt{s}$ (GeV)

Fig. 14

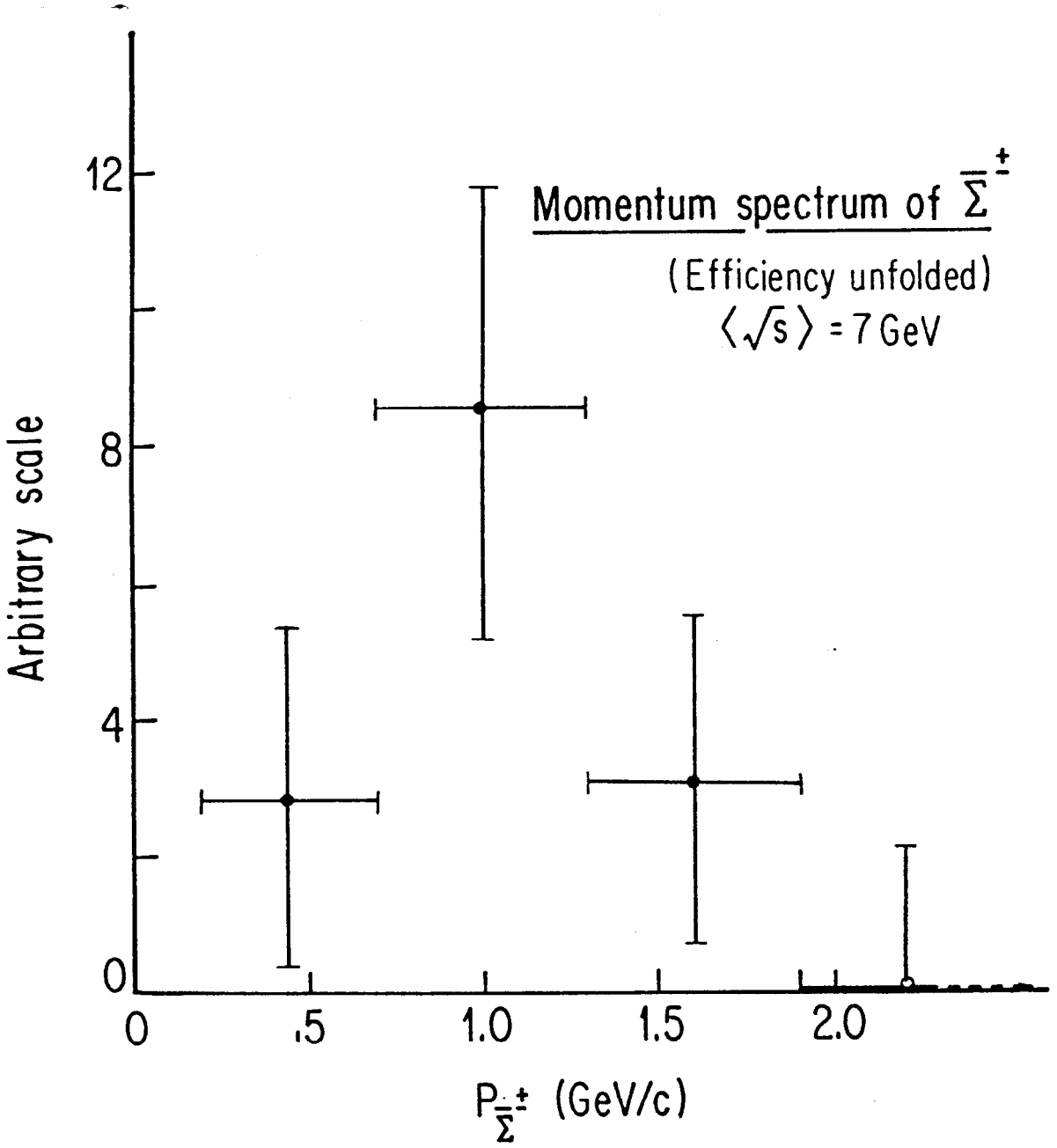
Momentum spectrum of $\bar{\Sigma}^{\pm}$
(Efficiency unfolded)
$\langle\sqrt{s}\rangle$ = 7 GeV
Arbitrary scale
12
8
4
0
0
.5
1.0
1.5
2.0
$P_{\bar{\Sigma}^{\pm}}$ (GeV/c)

Fig. 15

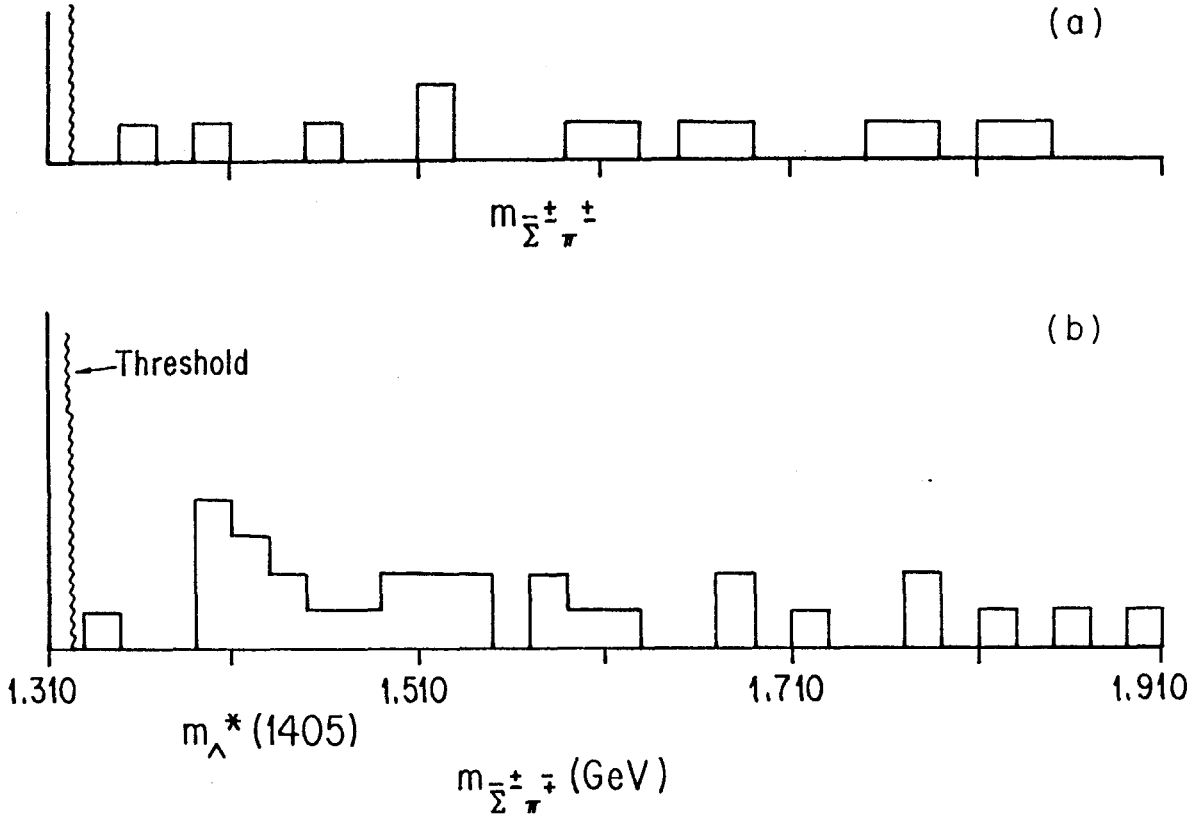
(a)
$m_{\bar{\Sigma}^{\pm}\pi^{\pm}}$
(b)
Threshold
1.310
1.510
1.710
1.910
m_{Λ}* (1405)
$m_{\bar{\Sigma}^{\pm}\pi^{\mp}}$ (GeV)

Fig. 16

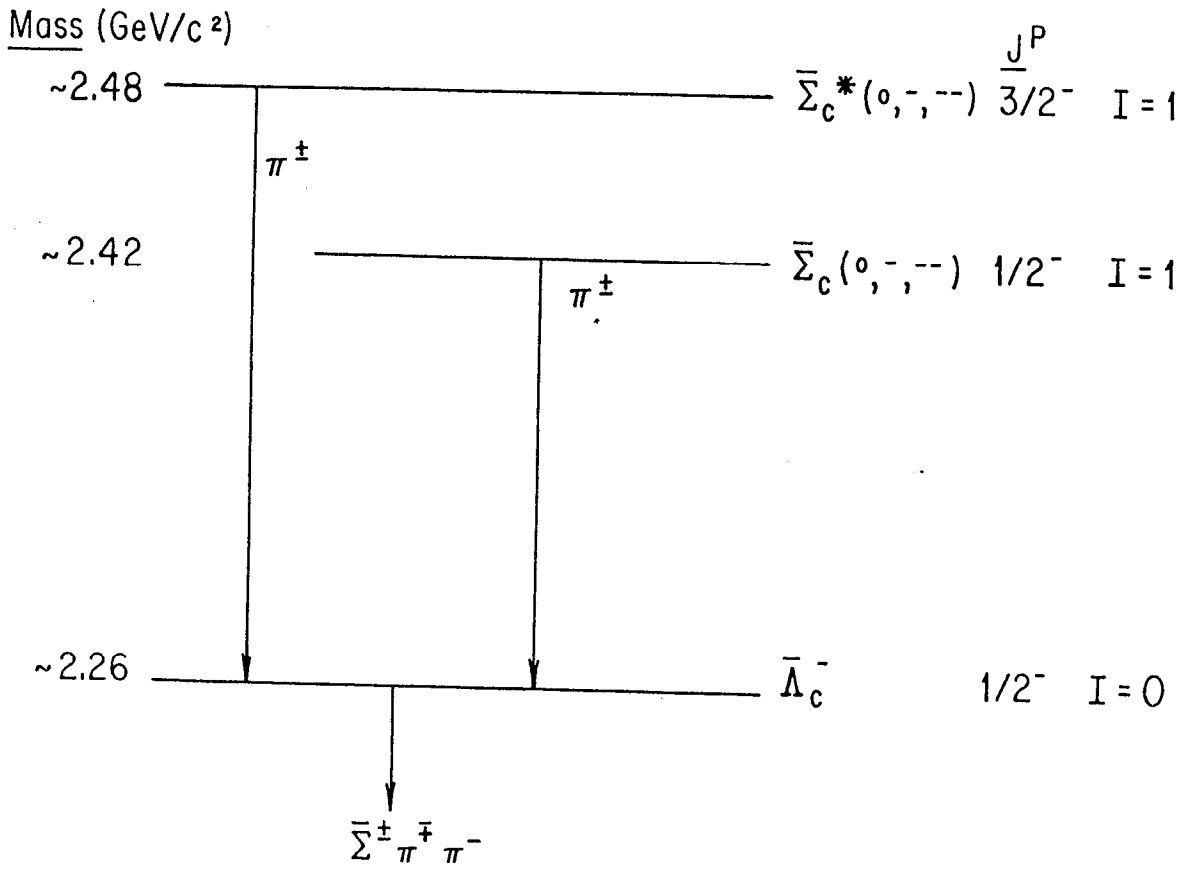
Mass (GeV/c²)
~2.48
~2.42
~2.26
$\bar{\Sigma}_c^*(0,-,--)$ J^P 3/2⁻ I = 1
$\bar{\Sigma}_c(0,-,--)$ 1/2⁻ I = 1
$\bar{\Lambda}_c^-$ 1/2⁻ I = 0
$\pi^\pm$
$\pi^\pm$
$\bar{\Sigma}^\pm \pi^\mp \pi^-$

Fig. 17

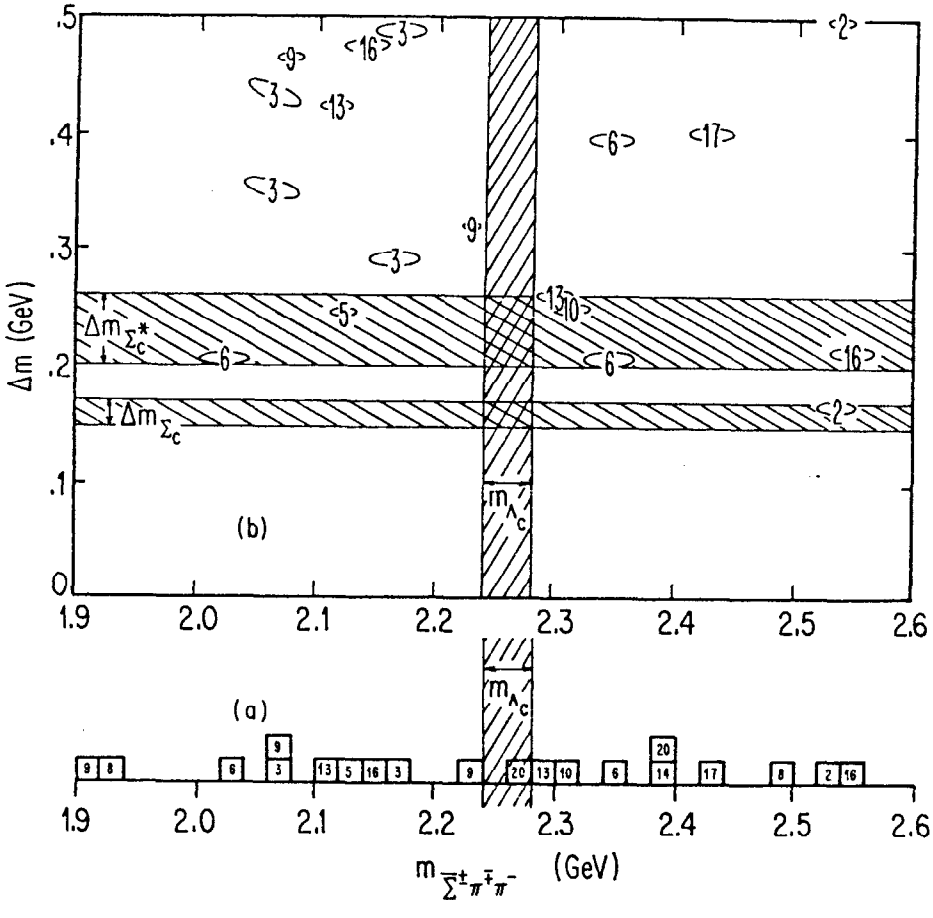
Δm (GeV)
.5
.4
.3
.2
.1
0
1.9
2.0
2.1
2.2
2.3
2.4
2.5
2.6
(b)
(a)
$\Delta m_{\Sigma_c^*}$
Δm_{Σ_c}
m_{Λ_c}
$m_{\overline{\Sigma}^{\pm}\pi^{\mp}\pi^-}$ (GeV)

Fig. 18